Core-edge 2D fluid modeling of full tokamak discharge with varying magnetic equilibrium: from WEST start-up to ramp-down

M Scotto d'Abusco, G Giorgiani, J F Artaud, H Bufferand, G Ciraolo, P Ghendrih, E Serre, P Tamain

Core-edge 2D fluid modeling of full tokamak discharge with varying magnetic equilibrium: from WEST start-up to ramp-down

M. Scotto d'Abusco[1, 2], G. Giorgiani[1], J.F. Artaud[2], H. Bufferand[2], G. Ciraolo[2], P. Ghendrih[2], E. Serre[1], P. Tamain[2].

[1] Aix-Marseille Univ., CNRS, Centrale Marseille, M2P2, Marseille, France
[2] CEA, IRFM, F-13108, St Paul-lez-Durance, France

Abstract. In the present work we investigate for the first time the 2D fluid transport of the plasma in WEST during an entire discharge from the start-up to the ramp-down (shot #54487). The evolution of density profile, electron and ion temperatures together with the experimental magnetic equilibrium, total current and gas-puff rate is investigated. Comparisons with the interferometry diagnostic show a remarkable overall qualitative agreement during the discharge that can be quantitative at some locations in the plasma core. If at the onset of the X-points during the ramp-up the electron heat flux is dominant at the target, present results show that the ion heat flux becomes dominant during the stationary phase of the discharge. Using a simple model for erosion, present results assess the tungsten sputtering due to deuterium ions during the start-up and ramp-up phases of the discharge and confirms the need to consider full discharge simulation to accurately treat the W source of contamination. This work also demonstrates the interest of developing magnetic equilibrium free solver including efficient time integration to step toward predictive capabilities in the future for fusion operation.

1. Introduction

With the perspective of ITER burning plasma operation, the control of heat and particle fluxes at the plasma facing components becomes critical. Most of the studies focus on steady-state regimes during the main heating phase at high plasma current where fusion reactions take place. However, characterizing and modelling the features of the full tokamak discharge from start-up to ramp-down are particularly important for scenario preparation in order to guarantee optimal operation and the safety of the reactor. Large uncertainties remain on the plasma transport and boundary evolution as well as on the existence of a safe operation scenario to reach the high performance steady-state regime during plasma current ramp-up and ramp-down phases prior to entering or leaving the burning phase plasma. During the ramp-up phase, the current is progressively increased

in the machine to a plateau value, usually mainly by inductive means. This phase is critical to give a fast and robust access to the target flat-top scenario (safety factor profile tailoring for high confinement scenarios or to prevent detrimental MHD events) [1]. The issue of ITER startup has been discussed in detail in the ITER Physics Basis [2–4]. In the ITER reference scenario the plasma is initially limited on two discrete beryllium limiters on the low eld side (LFS) before expanding progressively with the plasma current and density ramp-up to its fully diverted shape. In a metallic environment, that may be a critical phase for erosion associated to the sputtering of impurities.

The competition between ohmic heating and impurities radiation is then particularly important to describe during this phase. Moreover light impurities also play a role in determining the current profile and thus ohmic heating through changes in the resistivity. After the main heating phase, the plasma current and energy content must also ramped down smoothly to end the burning phase safely. Thus, for a successful tokamak operation, all plasma properties must be characterized as accurately as possible during all these phases.

The difficulty to get global experimental measurements requires obtaining complementary and reliable numerical results from simulations to support experimental data analysis, and with the ultimate goal to reach a predictive capability to design optimized scenarios. To our knowledge, current simulations related to full discharge are performed by means of integrated modelling based on 1D transport codes (see for example in [5–7]) for fast-time execution during the operation. In such approach, the plasma density is assumed to increase linearly, and the effective charge decreases monotonically as the density increases [8] while the heat transport is assumed to follow an ohmic energy confinement time scaling law [9]. More comprehensive simulations are nevertheless mandatory to accurately characterize all plasma properties during the full discharge.

Despite the constant increase of the computational power, 2D transport codes remain standard in the international community to investigate turbulent transport during the main steady heating phase in realistic tokamak geometries. These reduced models, based on averaged fluid Braginskii equations and assuming axisymmetry of the plasma, are indeed well adapted to provide relevant information on appropriate return times, particularly at the plasma edge, in a flow region that encompasses closed and open magnetic field lines and extends up to the tokamak wall. There exists a number of 2D codes for engineering purpose (see for example in [10–12]) that can be eventually coupled to other codes to take into account additional equations describing the dynamics of neutrals or impurities produced by the plasma refueling and plasma wall interactions. However these codes can not address efficiently all phases of the discharge due to numerical limitations. Generally based on first and second order finite differences / finite volumes, and so structured meshes, their discretization is aligned along the magnetic field lines to take advantage of the transport features [13]. This makes challenging to describe accurately the tokamak wall for realistic geometry as well the plasma flow around magnetic singularities like the X-point. Moreover, that prevents

the simulation of non-stationary magnetic configurations that requires a very expensive on the fly re-meshing of the computational domain. To overcome these limitations we have recently proposed a 2D high-order hybrid discontinuous Galerkin finite-element solver (HDG) [14, 15]. Implemented into the well-known SolEdge3X suite of codes [12] (new release of SolEdge2D-EIRENE), SolEdge3X-HDG currently allows to perform accurate 2D fluid transport simulations for versatile magnetic equilibrium and tokamak wall geometries. The high-order unstructured meshes in the whole tokamak cross-section guarantee a low numerical dissipation despite the nonalignment of the discretization [16]. Taking into account particle and energy sources as realistic as possible remains one of the major issues for plasma modeling in order to get reliable simulations. Plasma-wall interactions lead to the injection of neutrals and impurities into the plasma, constituting sources or sinks for energy and matter that impact the plasma equilibrium as well as the tokamak performance [17]. Different modules including more or less rich physics have been developed and coupled with plasma solvers to predict their transport. One of the most complete model in the fusion community is certainly the EIRENE code [18] in which the distribution of neutrals as well as the corresponding sources of energy and matter for the plasma solver are computed relying on kinetic Boltzmann model and a Monte-Carlo method. While providing a rich description of the physics, such a complete approach may lead to very slow convergence rates, mostly in higher density regime where the collisional process start to be relevant, and thus can be very penalizing for the global transport code performance. This is even more true in large size tokamak like JT60 SA or ITER. This very demanding computational resource has encouraged the community to develop faster reduced models for neutrals based on fluid or hybrid fluid/kinetic approach [19, 20] able to simulate in many cases the main flow features in reasonable agreement with the fully kinetic results.

Moreover, to bring and to sustain plasma to the temperature necessary for fusion, different sources of external heating have to be used in a tokamak that have to be modelled as accurately as possible in the codes. In ITER, electron will be heated by neutral beam injection and high-frequency electromagnetic waves that will complement ohmic heating produced by the high intensity current induced by the magnetic field through induction (https://www.iter.org/mach/heating).

The WEST tokamak is intended to be a test bed for ITER in order to explore different scenarios for the transition to H-mode in deuterium plasmas, and to observe the interaction with the divertor's tungsten elements, particularly when operating in helium [21]. In the present paper, we simulate 2D transport in the whole cross-section of WEST and for a full discharge, i.e. including the start-up, the ramp-up, the flat-top and the ramp-down. The magnetic equilibrium as well as the gas puff time evolution are extracted from the WEST experimental database.

The manuscript is organized as follows: the physical and numerical model are first introduced in Sec 2 and 3. In particular, the self-consistent sources of particle and heat based on a diffusive fluid model for neutrals and an ohmic heating mechanism for the energy source are introduced. Then a careful verification and codes benchmarking

with the state-of-the-art 2D transport code Soledge3X [22] in WEST configuration is provided in Sec. 4, in order to show the capability of the code to provide results of reference despite the nonalignment of the numerical discretization with the magnetic field lines. Results of full WEST discharge are finally analyzed in Sec 5, showing the need to take into account the transient phases of the magnetic equilibrium to tend towards predictive capability. Concluding remarks and perspectives are summarized in Sec. 6.

2. The physical model

The physical model is based on the Braginskii conservative equations for density, parallel momentum, total energy for singly charged ions and electrons in the entire volume of plasma expanding from the core to the wall of a realistic tokamak. With the ultimate goal to take into account realistic and self-consistent sources for particles and energy, neutral dynamics and ohmic heating are considered. Note, however, that the plasma current is not an unknown of the problem but it is prescribed from the experiment and taken into account in the ohmic heating source term only. A magnetic field $\boldsymbol{B}$ with a toroidal and poloidal component ($||B_p|| << ||B_t)||$) is prescribed that encompasses both closed and open flux surfaces. It defines privileged flow directions along which the governing equations are projected using the differential operators $\boldsymbol{\nabla}_{||} = \boldsymbol{b} \cdot \boldsymbol{\nabla}$ and $\boldsymbol{\nabla}_{\perp} = \boldsymbol{\nabla} - \boldsymbol{b} \cdot \boldsymbol{\nabla}$, where $\boldsymbol{b} = \frac{\boldsymbol{B}}{||\boldsymbol{B}||}$, is the unitary vector in the direction parallel to the magnetic field.

2.1. The 2D drift-reduced two-fluid equations

The quasi-neutrality and the quasi-ambipolarity assumptions lead to the density $n_e \approx n_i \approx n$ and the parallel velocity $u_e \approx u_i \approx u$ (as mentionned above the plasma current is not taken into account here). Neglecting the electron inertia ($m_e/m_i = O(10^{-3})$, m_e and m_i being the mass of the electrons and ions, respectively) the expression for the parallel electric field is given by $enE_{||} = -\nabla_{||}(nk_bT_e)$, with k_b the Boltzmann constant. Under these assumptions the system of equations for a non-isothermal plasma of density, parallel velocity, electrons and ions temperatures n, u, T_e, T_i, respectively, writes :

$$\partial_t n + \nabla \cdot (nu\mathbf{b}) - \nabla \cdot (D\nabla_{\perp} n) = S_n \tag{1}$$

$$\partial_t (m_i nu) + \nabla \cdot (m_i nu^2 \mathbf{b}) + \nabla_{\|}(k_b n(T_e + Ti)) - \nabla \cdot (\mu \nabla_{\perp}(m_i nu)) = S_{\Gamma} \tag{2}$$

$$\begin{aligned}
&\partial_t\left(\frac{3}{2}k_b n T_i + \frac{1}{2}m_i n u^2\right) + \nabla\cdot\left(\left(\frac{5}{2}k_b n T_i + \frac{1}{2}m_i n u^2\right)u\mathbf{b}\right) - nueE_\parallel \\
&- \nabla\cdot\left(\frac{3}{2}k_b(T_i D\nabla_\perp n + n\chi_i\nabla_\perp T_i)\right) - \nabla\cdot\left(-\frac{1}{2}m_i u^2 D\nabla_\perp n + \frac{1}{2}m_i\mu n\nabla_\perp u^2\right) \\
&- \nabla\cdot(k_{\parallel i}T_i^{\frac{5}{2}}\nabla_\parallel T_i\mathbf{b}) + \frac{3}{2}\frac{k_b n}{\tau_{ie}}(T_e - T_i) = S_{E_i}
\end{aligned} \tag{3}$$

$$\begin{aligned}
&\partial_t\left(\frac{3}{2}k_b n T_e\right) + \nabla\cdot\left(\frac{5}{2}k_b n T_e u\mathbf{b}\right) + nueE_\parallel - \nabla\cdot\left(\frac{3}{2}k_b(T_e D\nabla_\perp n + n\chi_e\nabla_\perp T_e)\right) \\
&- \nabla\cdot(k_{\parallel e}T_e^{\frac{5}{2}}\nabla_\parallel T_e\mathbf{b}) - \frac{3}{2}\frac{k_b n}{\tau_{ie}}(T_e - T_i) = S_{E_e}
\end{aligned} \tag{4}$$

D, μ, χ_i and χ_e are ad hoc diffusion coefficients that take into account the collisional transport and turbulent effects in the cross field direction. They have been estimated either by experiments or by numerical turbulent simulations, and they are usually chosen less or equal to 1 $m^2 s^{-1}$. Regarding the current status of the solver development, they must be constant and equal in the whole computational domain, $D = \mu = \chi_i = \chi_e$. $(k_{||,i}T_i^{\frac{5}{2}})$ and $(k_{||,e}T_e^{\frac{5}{2}})$ are the nonlinear parallel diffusions for ion and electron, respectively. The parallel diffusion coefficients [23] depend on the mass of the species and are equal for the deuterium to $k_{\parallel i} = 60$ $[Wm^{-1}eV^{-7/2}]$ and $k_{\parallel e} = 2000$ $[Wm^{-1}eV^{-7/2}]$. τ_{ie} is the relaxation time for the collisional coupling term between electrons and ions with $W = \frac{3}{2}\frac{k_b n}{\tau_{ie}}(T_e - T_i)$. $S_n, S_\Gamma, S_{E_i}, S_{E_e}$ denote the density, momentum, and energies source terms respectively.

2.1.1. Boundary Conditions The system above is supplemented with appropriate boundary conditions modeling the plasma-wall interaction. The Bohm boundary condition are used in the parallel direction that leaves free the density value at the wall and forces an outgoing sonic/supersonic velocity:

$$\begin{aligned}
u \geq c_s \qquad if \quad \mathbf{b}\cdot\mathbf{n} > 0 \\
u \leq -c_s \qquad if \quad \mathbf{b}\cdot\mathbf{n} < 0
\end{aligned} \tag{5}$$

where $\boldsymbol{n}$ is the outer normal to the surface and $c_s = \sqrt{k_b(T_i + T_e)/m_i}$ the plasma sound speed. $M = u/c_s$ defines the parallel Mach number. For ion and electron energy equations, the Bohm condition imposes the parallel fluxes to the sheath transmission values, that leads to:

$$\begin{aligned}
(nE_i + p_i)u - k_{\parallel i}T_i^{5/2}\nabla_\parallel T_i = \gamma_i u p_i + \frac{1}{2}n m_i u^3 \\
(nE_e + p_e)u - k_{\parallel e}T_e^{5/2}\nabla_\parallel T_e = \gamma_e u p_e
\end{aligned} \tag{6}$$

where $\gamma_i = 2.5$ and $\gamma_e = 4.5$. p_i and p_e are the ion and electron pressures $[m^{-1}s^{-2}]$ equal to nk_bT_i and nk_bT_e, respectively. E_i and E_e are the ion and electron energies $[m^2s^{-2}]$ equal to $\frac{3}{2}k_bT_i + \frac{1}{2}m_iu^2$ and $\frac{3}{2}k_bT_e$, respectively

2.2. Modelling of self-consistent sources of particles and energy

The development of a diffusive model for neutrals and of an ohmic heating source term is proposed for the self-consistent treatment of the sources.

2.2.1. A diffusive model for neutrals In the context of developing reduced fluid model for neutrals [20, 24] we propose in this work a simple diffusive model to evaluate the neutral density n_n. Despite its overall simplicity, this reduced model is appropriate for understanding the effect of the ionization source on the plasma flows on the divertor target [25]. It allows to get a rather realistic description of the plasma in front of the target and, thanks to the recycling process at the wall, it provides a self-consistent source of particle which is required to get a more reliable particles balance in the simulations. The additional equation to solve writes as:

$$\partial_t n_n - \nabla \cdot (D_{n_n} \nabla n_n) = S_{n_n,iz} + S_{n_n,rec} + S_{n_n} \tag{7}$$

where D_{n_n} is the neutral diffusion coefficient derived from Ref. [20] and by assuming that the neutral dynamics is dominated by the balance between the pressure gradient and the momentum source. Then, neglecting the convective and pressure tensor terms in the pressure diffusion equation given in Ref. [20] leads by rearranging the terms to:

$$D_{n_n} = \frac{eT(eV)}{m_i n(< \sigma v >_{cx} + < \sigma v >_{iz})} \tag{8}$$

where T is the temperature of neutrals assumed to be equal to T_i in the model, $< \sigma v >_{iz}$ and $< \sigma v >_{cx}$ are the ionization and charge exchange $< \sigma v >_{cx}$ cross section rates, respectively [26]. Eq. **??**In the present work this coefficient will be assumed to be constant. For typical plasma density of the order of 10^{19} m^{-3}, Eq. 8 leads to D_{n_n} of the order of 1000 $m^2 s^{-1}$.

The neutral flux is decreased and increased by ionization ($S_{n_n,iz}$) and recombination ($S_{n_n,rec}$) processes, respectively. S_{n_n} takes into account gas injection during standard tokamak operations when it is relevant. All the ionization-recombination-radiation terms that couple the plasma with neutrals are given in Appendix A.

The neutral flux is related to the plasma one through the boundary condition at the wall

$$-D_{n_n} \nabla n_n \cdot \mathbf{n} = -R\big(- D_n \nabla n \cdot \mathbf{n} + nu\mathbf{b} \cdot \mathbf{n}\big) \tag{9}$$

which states that a percentage of the plasma particle flux hitting the wall (diffusive plus convective) is recycled and re-injected as neutrals. The percentage is given by the recycling coefficient R which is a parameter of the simulation while $\boldsymbol{n}$ is the unit vector in the direction normal to the wall. $R = 1$ is an asymptotic value meaning that 100% of the plasma flux could be recycled at the wall and re-injected in form of neutrals. This value is however non physical since part of the recombined plasma remains trapped in the wall or pumped, and thus R is always chosen at a smaller value close to the unity.

This condition together with the continuity equation Eq. 1 and the diffusion equation Eq. 7 ensures the conservation of the total number of particle in the system.

2.2.2. The ohmic source of energy As a first step in the development and implementation of self-consistent sources of energy, we have taken into account the ohmic heating neglecting all other external sources of heating (RF, LW, ICRH). During the discharge, the current in the central solenoid changes in time producing variation of the magnetic flux in the poloidal cross section. The central solenoid plays a role of the primary circuits of a transformer and, according to the Lenz law, any change in the magnetic flux Φ_B generates a voltage $V = -\frac{d\Phi_B}{dt}$. Thus the plasma results inductively coupled with the transformer circuit and the power loss in the plasma due to the induced current can be described by Eq. 10:

$$S_{ohmic} = \eta j^2 = 0.51 \frac{m_e^{1/2} e^{1/2} ln\Lambda}{3(2\pi)^{3/2}\epsilon_0^2} \frac{1}{T_e^{3/2}} j^2 \tag{10}$$

where η is the plasma resistivity, whose expression is given by the collisional Spitzer Harm formulation [9], and j is the current density, whose distribution is taken by the experimental data. The ohmic heating mainly impacts the electrons because their small mass with respect to ions, $m_e/m_i << 1$. Thus the source term of Eq. 10 has been only implemented in the equation for the electron energy Eq. 4. In the present simulations, the density current profile is extracted from experimental data.

3. Numerical model

In Soledge3X-HDG, the 2D Braginskii equations (Eqs. 1-4) are resolved implicitly in time using a high-order finite elements discretization based on a Hybrid Discontinuous Galerkin (HDG) method. Both triangles and quadrangles can be used for the mesh. This discretization is thus magnetic equilibrium free that allows it to deal accurately with non steady magnetic equilibrium without remeshing [27], as well as with tokamak wall geometry of any complexity. Moreover, magnetic singularities do not required any specific treatment that allows us to expand easily the computational domain to the entire tokamak cross-section or to discretize accurately the plasma flow regions around X-points.

All technical details are described in Appendix C. Eqs. 1-4 are written in terms of conservative variables, introducing the vector $\boldsymbol{U} = \{U_1, U_2, U_3, U_4\}^T = \{n, nu, nE_i, nE_e\}^T$ (the superscript T stands for transpose). As a first step a local problem is solved in each element of the finite-element discretization using a weak formulation to express the discrete unknowns $\boldsymbol{U}$ at the element nodes in terms of another approximation of the solution, called the trace solution $\hat{\boldsymbol{U}}$, which is defined on the borders of the element. The second step of the HDG solution consists in setting up a global problem which allows to obtain $\hat{\boldsymbol{U}}$ in the whole mesh skeleton. The global problem is obtained by imposing in a weak form the continuity of the uxes across the

borders of the elements. Once $\hat{\boldsymbol{U}}$ is obtained, it is possible to recover the elementary solution $\boldsymbol{U}$ on each element using a local post processing. The introduction of $\hat{\boldsymbol{U}}$ dened only on the borders of the elements leads to a linear system of smaller size than in a classical discontinuous Galerkin method. This is particularly interesting when using finite-elements of high-order.

The time discretization is fully implicit, and the non-linear terms are linearized using a classic Newton-Raphson method. A steady-state version of the code is also implemented solving B.1 without the time derivative terms.

4. Verification and codes benchmarking

The code verification is performed using the method of the manufactured solution in the WEST geometry. The code is then benchmarked with the well-referenced code SolEdge3X [12, 22] in its 2D transport version (new release of SolEdge2D-EIRENE), for both limited plasma in a circular geometry and diverted plasma in the WEST geometry. Eqs. 1-4 are resolved until steady state using the same magnetic equilibrium, and neither neutrals nor Ohmic heating are taken into account here.

4.1. Manufactured solutions

In 2D computational domains Ω as shown in Fig. 1 the following analytical solution is considered for all variables:

$$\begin{array}{lll} n = 2 + sin(2\pi x)sin(2\pi y) & u = cos(2\pi x)cos(2\pi y) & [x,\ y] \in \Omega \\ E_i = 20 + cos(2\pi x)sin(2\pi y) & E_e = 10 - sin(2\pi x)cos(2\pi y) & \end{array} \tag{11}$$

where x and y are the Cartesian coordinates directed along the horizontal and vertical axis respectively.

In order to make it solution of the system, appropriate source terms $S_n,\ S_\Gamma,\ S_{E_i}$ *and* S_{E_e} are analytically calculated and implemented on the right and hand side of Eqs. 1-4.

The tests are performed on unstructured triangular meshes as shown on Fig. 1. All the boundary conditions are of Dirichlet type. Finally, the divergence free poloidal magnetic field is chosen as:

$$b_x = \frac{1}{30}(x - y^2 + 2)$$
$$b_y = \frac{1}{30}(xy + y)$$

where b_x and b_y are the Cartesian components of the magnetic field directed along the horizontal and vertical axis respectively. Here $D = \mu = \chi_i = \chi_e = 1\ m^2 s^{-1}$

Convergence tests are performed refining the mesh by dividing per two the characteristic length (h) of each element inside the element of the coarser mesh (see

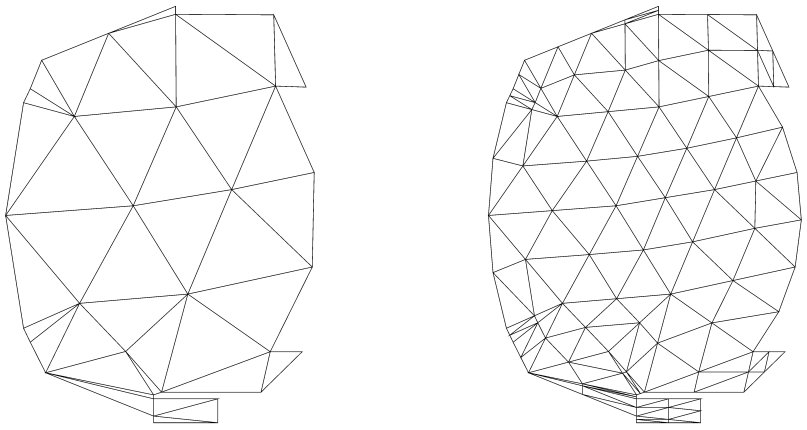

(a) $h = 4 \times 10^{-2}$ (b) $h = 2 \times 10^{-2}$

Figure 1: Examples of two triangles meshes used in the WEST geometry with the method of the manufactured solution.

Fig. 1a and Fig. 1b). Thus $h = 1/2^m$, for $m = 1, ..., 5$. The tests are performed for different orders of interpolation with $p = 1, ..., 4$. Results are shown on Figs. 2, and show the expected theoretical convergence slope $p+1$ whatever the polynomial degrees.

4.2. Codes benchmarking with SolEdge3X

SolEdge3X [12, 22] is based on a finite-volume discretization and on a flux aligned approach. Therefore, boundary conditions at the tokamak wall are applied using an immersed boundary technique [28]. In all simulations cross-field diffusion coefficients are taken equal to $D = \mu = \chi_i = \chi_e = 1\ m^2/s$ while the parallel diffusion coefficients $k_{||,i}$ and $k_{||,e}$ and the temperature relaxation time τ_{ie} are computed considering a deuterium plasma, see Ref.[23]. As expected by its integration scheme, SolEdge2D-HDG is here about 10 times faster than SolEdge3X to converge towards the steady state (1.2 hours on 32 cpu).

4.2.1. Geometries and meshes The computational domains correspond to the flow regions at the plasma edge, that encompass open and closed magnetic field lines including the separatrix.

In the circular configuration, a structured quadrangular mesh of 1120 $p = 4$ elements and an unstructured quadrangular mesh of 2522 $p = 4$ elements have been used Figs. 3a, b. In the corresponding SolEdge3X simulations the mesh is composed by 10800 cells with one point per cell.

In the WEST configuration, the present computations use an unstructured grid composed by 10816 $p = 4$ elements, Fig. 3c. In the corresponding SolEdge3X simulations the mesh is composed by 28220 cells.

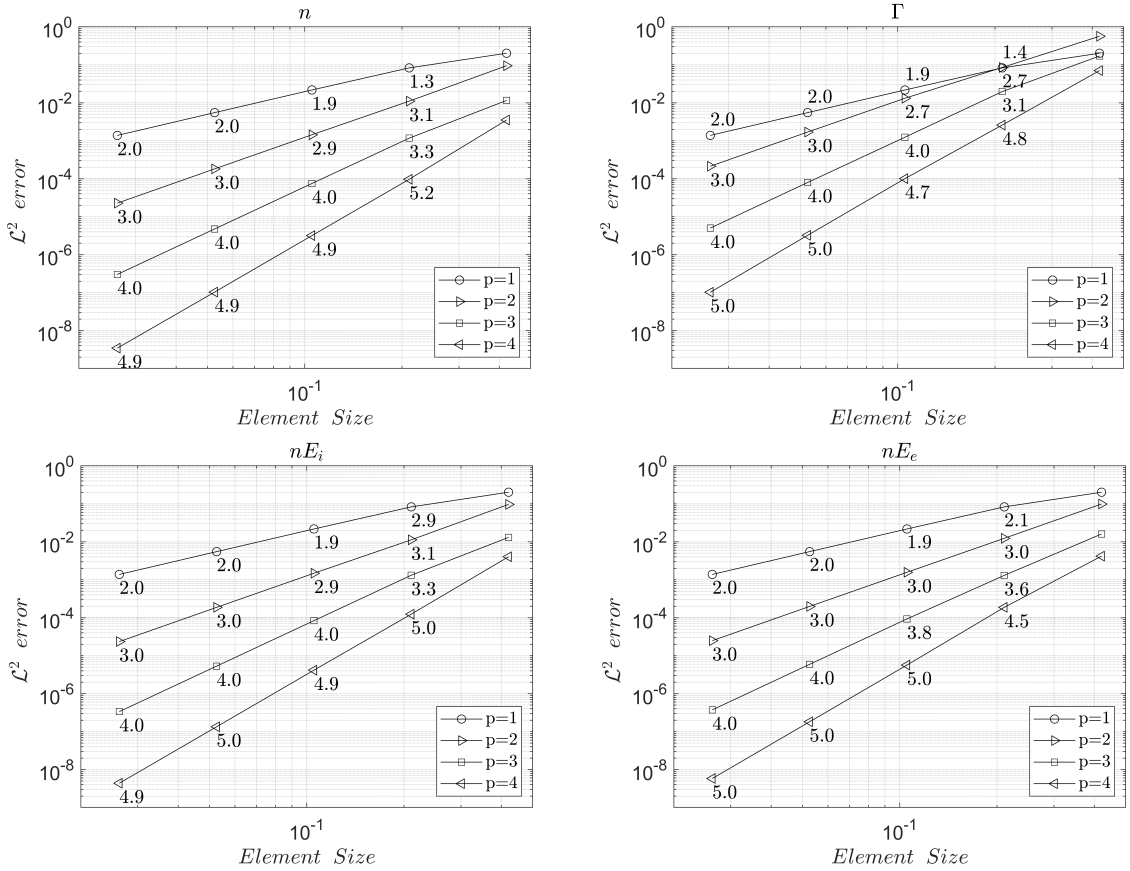

Figure 2: Convergence plots of the L^2-error with respect to the finite-elements size h for the four conservative variables and for various polynomial degrees p. The slope of the curves is provided for each mesh. The L^2-error is defined on all nodes of the mesh as $\sqrt{\int(\mathbf{U}-\mathbf{U_a})^2}$ where $\mathbf{U}$ is the vector of conservative variables and $\mathbf{U}_a$ is the analytical solution of Eq.11.

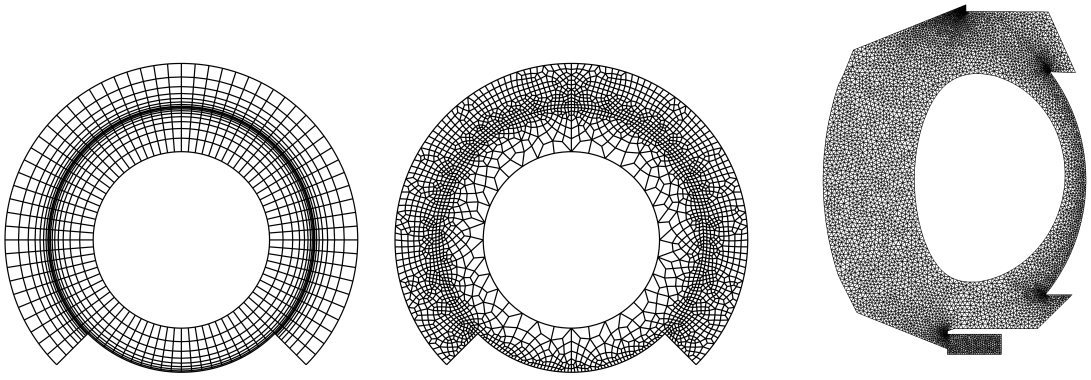

(a) Aligned quad-mesh (b) Non aligned quad-mesh (c) Non aligned WEST triangle-mesh

Figure 3: Examples of aligned (a) and non aligned (b, c) meshes for circular-limited (a, b) and WEST (c) geometries of the edge and SOL region around the separatrix.

4.2.2. Magnetic equilibrium In the circular geometry (Figs. 3a, b), the following analytic magnetic equilibrium is used:

$$\begin{aligned} B_r(r,\theta) &= -B_0 \frac{r}{qR(r,\theta)\sqrt{1-\left(\frac{r}{R_0}\right)^2}} sin(\theta) \\ B_z(r,\theta) &= B_0 \frac{r}{qR(r,\theta)\sqrt{1-\left(\frac{r}{R_0}\right)^2}} cos(\theta) \\ B_\phi(r,\theta) &= \frac{B_0 R_0}{R(r,\theta)} \end{aligned} \tag{12}$$

where B_r and B_z are the magnetic field components directed along the horizontal and vertical axis respectively, while B_ϕ is aligned with the torus axis.

$r \in [0.5,\ 1]$ is the radial coordinate of the little radius, $R_0 = 2\ m$ is the major radius and $q = cost = 4$ is the safety factor. The 2D computation domain is centered around $\boldsymbol{x} = (R_0,\ 0)$ and $R(r,\theta) \in [1,\ 3]\ m$ defines the radial coordinate along the horizontal axis. The value of B_0 is not relevant because the equations only depends on $\boldsymbol{b} = \left(\frac{B_r}{|\boldsymbol{B}|}, \frac{B_\theta}{|\boldsymbol{B}|}\right)$.

In WEST geometry, the magnetic equilibrium is extracted from an experimental 2D map of $B_r,\ B_z,\ B_\phi$ during the steady state as the one shown on Fig. 9c. A 2D bilinear interpolation is used to estimate the values of the magnetic field on the nodes of the mesh.

4.2.3. Boundary conditions In the circular configuration, the magnetic field is always tangent to the tokamak wall as well as on the limiter roof, so a simple homogeneous Neumann boundary condition is applied ($\partial_\perp = 0$) there. At the core, boundary Dirichlet conditions are used for the density, the parallel velocity and the temperatures with $n = 1e19,\ u = 0,\ T_{i,e} = 50\ eV$. Finally, at the limiter sidewall an outgoing supersonic velocity is forced as prescribed by the Bohm boundary conditions. In WEST geometry, Bohm conditions are applied everywhere at the outer boundary of the domain (tokamak wall) and at the limiter sidewall

4.2.4. Results of the comparisons In the circular geometry, both codes provide the 2D maps of the solution with all expected features as shown on Fig. 4. The solution is poloidally symmetric for the density (Fig. 4a) and thermal energies (Figs. 4c, d), which is consistent with a much smaller crossfield than parallel transport. As observed experimentally, the heat transport also appears to be in the sheath limited regime [23]. The density and temperatures are maximum at the core boundary where Dirichlet boundary conditions are applied. As expected, all quantities decrease radially beyond the separatrix into the SOL, as it will be confirmed below on the low field side (LFS) mid-plane profiles on Fig. 5. The parallel Mach number M is expected to be poloidally antisymmetric with a stagnation point at the top since the transport is poloidally symmetric. However, one can also observe some differences, for instance a

supersonic flow pattern on the HFS [29], while the flow remains subsonic on the LFS. This effect has been analyzed in previous work [12] and shown to be governed by the variations of the magnetic field amplitude.

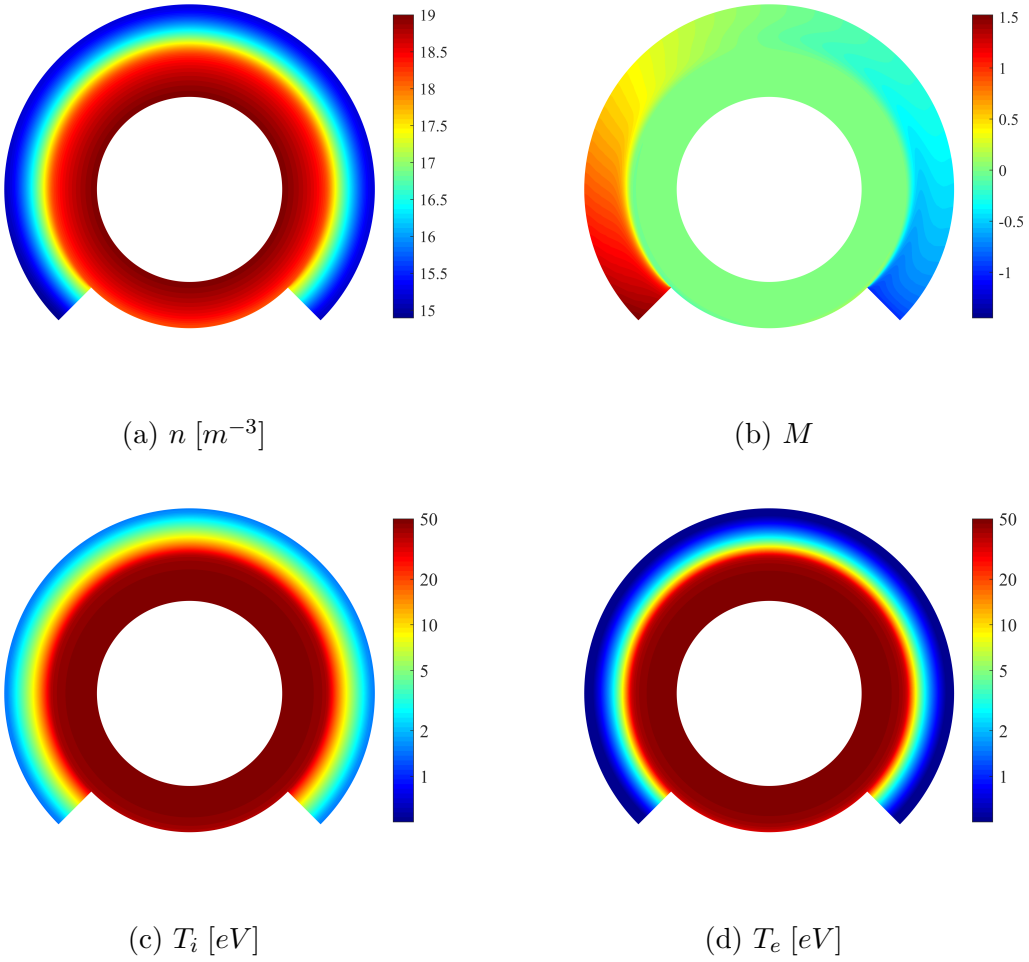

(a) n $[m^{-3}]$ (b) M

(c) T_i $[eV]$ (d) T_e $[eV]$

Figure 4: 2D maps of the solution in log scale in the circular-limited configuration using the aligned mesh of Fig. 3a: density n (a), parallel Mach number Ma (b), ion temperature T_i (c) and electron temperature T_e (d).

The comparison of the LFS mid-plane profiles for the density, and for the ion and electron temperatures on Fig. 5 allows a more quantitative comparison between the solutions. The overall agreement for all profiles is very good. The results show that the use of a non-aligned discretization on an unstructured mesh, thus independent of the magnetic equilibrium, does not impact the solution. The agreement with the Soledge3X solutions is very good in the close field lines region while a very small difference can be noticed in the SOL. A reasonable explanation relies on the use of two different closures for the parallel collision forces and heat fluxes. The present HDG solver incorporates the standard Braginskii closure which prescribes a energy exchange term that is proportional to $n^2/T^{3/2}$ and a parallel diffusion coefficient for the electrons that is about 30 times than

for the ions (see eq. 3 and eq. 4). Differently, in SolEdge3X a Zhdanov closure has been implemented, which computes the heat fluxes and the collisional forces in between the different species as a linear combination of parallel velocities and parallel temperature gradients as described in [22]. A smaller heat equipartition term in SolEdge3X than used here explains the small difference observed in the mid-plane temperature profiles.

The results show that the temperature decreases more rapidly for the electron than the ion with a shorter decay length λ_T in the SOL. This radial decay length results from a balance between radial and parallel transport. The latter is regulated by the sheath losses. It is thus a complex nonlinear and global mechanism. An analytical estimate can be however provided by a simplified 2D SOL description assuming a conductive dominated regime and integrating the energy balance equation along the parallel direction. This provides the order of magnitude of this e-folding length with $\lambda_{T_{i,e}} = \sqrt{\chi_{i,e} L_\parallel / (2\gamma_{i,e} c_s)}$, with in the current work $\gamma_i = 2.5, \gamma_e = 4.5$ and $\chi_i = \chi_e$. The SOL e-folding length values measured on Fig. 5 agree quite well with the theoretical estimates. For instance, close to the separatrix, an approximate calculation yields $\lambda_{T_i} = 5.10^{-2} m$ while $\lambda_{T_i} = 6.10^{-2} m$ from the simulation on Fig. 5. A similar agreement is found for λ_{T_e}. However, the actual SOL profiles can only be recovered with the full 2D transport model since the variations of the thermal energies, reducing the parallel transport, govern an increase of the e-folding length.

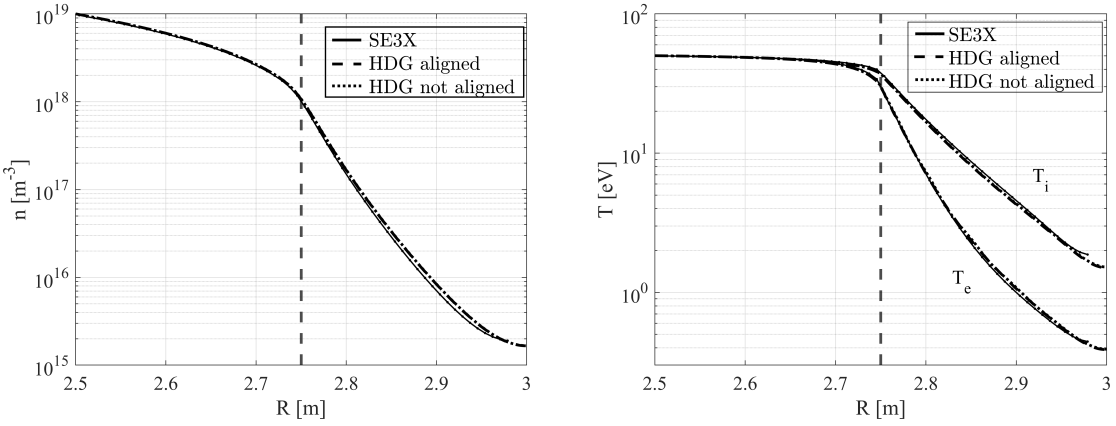

Figure 5: LFS mid-plane profiles for the density (a) and the temperatures (b). SolEdge3X (solid line) solution and SolEdge3X-HDG solutions using an aligned (dash line) or a non-aligned (dot line) mesh in the circular geometry.

In the WEST diverted geometry, additional numerical complexities come from the tokamak wall geometry as well as from the X-point singularity on the magnetic equilibrium that can be more efficiently handled by the unstructured non aligned approach than with SolEdge3X.

The comparison of the solutions obtained with the two codes is shown on Fig. 6. The solutions show a close qualitative agreement. A similar trend is observed for the

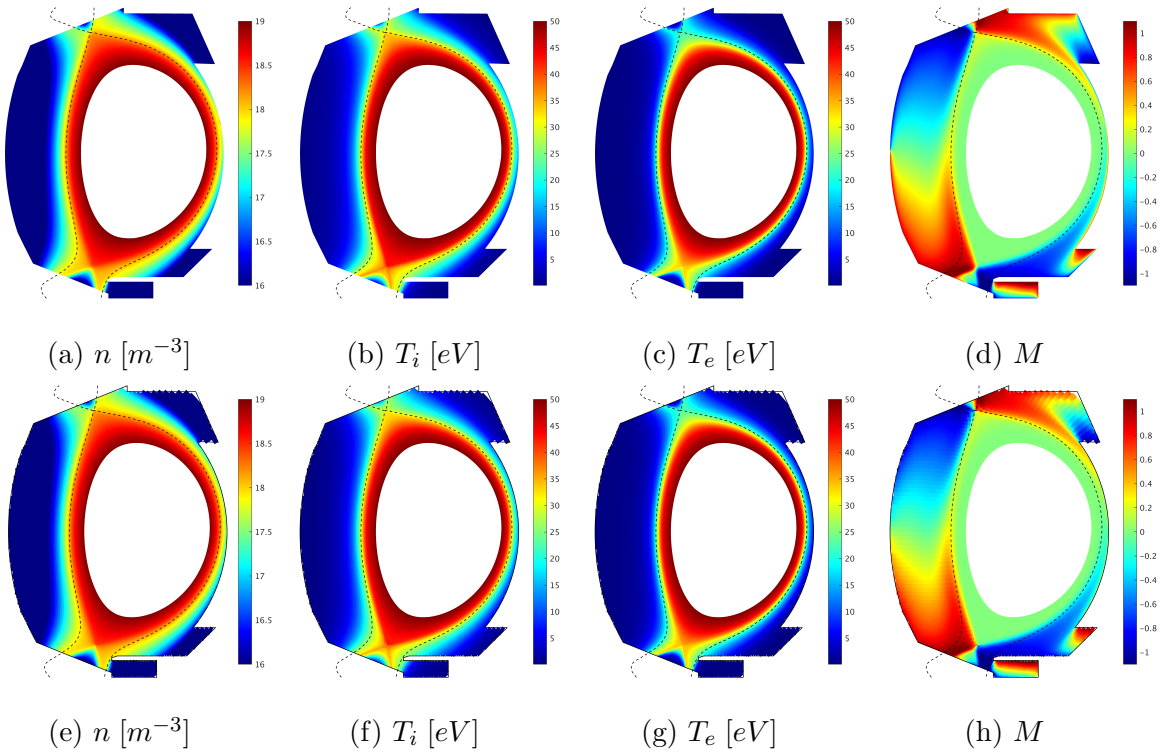

(a) n $[m^{-3}]$ (b) T_i $[eV]$ (c) T_e $[eV]$ (d) M

(e) n $[m^{-3}]$ (f) T_i $[eV]$ (g) T_e $[eV]$ (h) M

Figure 6: 2D maps of the solutions in the WEST configuration in log scale for the plasma density n (a, e), the ion temperature T_i (b, f), the electron temperature T_e (c, g) and the parallel Mach number Ma (d, h). (a, b, c, d) SolEdge3X-HDG solution, (e, f, g, h) SolEdge3X solution.

parallel Mach number M, with the same flow regions of positive and negative Mach number values as well as a flow reversal at the mid-plane positions. Both codes predict a slightly supersonic transition at the divertor legs position as prescribed by the theory related to the Bohm boundary condition [23]. Unlike the limiter case, one can observe in the WEST case parallel variations of the thermal energies typically by a factor 2 indicating that the simulation is performed at the transition from sheath limited to high recycling regimes.

A more quantitative analysis is allowed by comparing the LFS mid-plane profiles of the plasma quantities as well as the parallel profile for the Mach number M along the separatrix obtained with the two codes. Fig. 7a and Fig. 7b show a near perfect match for the density LFS mid-plane profiles, while for the temperature profiles a little mismatch remains in the SOL. It is a similar behaviour than observed in the circular configuration with a similar explanation related to the different closures used in the two codes for the parallel heat flux and the energy exchange term. In this configuration the SolEdge3X solution exhibits larger equipartition between ions and electrons than the HDG solution. A geometrical effect is also visible near the wall. Just at the front of the wall, the SolEdge3X-HDG solution shows a sharper decrease of the density and the temperatures than the SolEdge3X solution. This can be related to the wall discretization

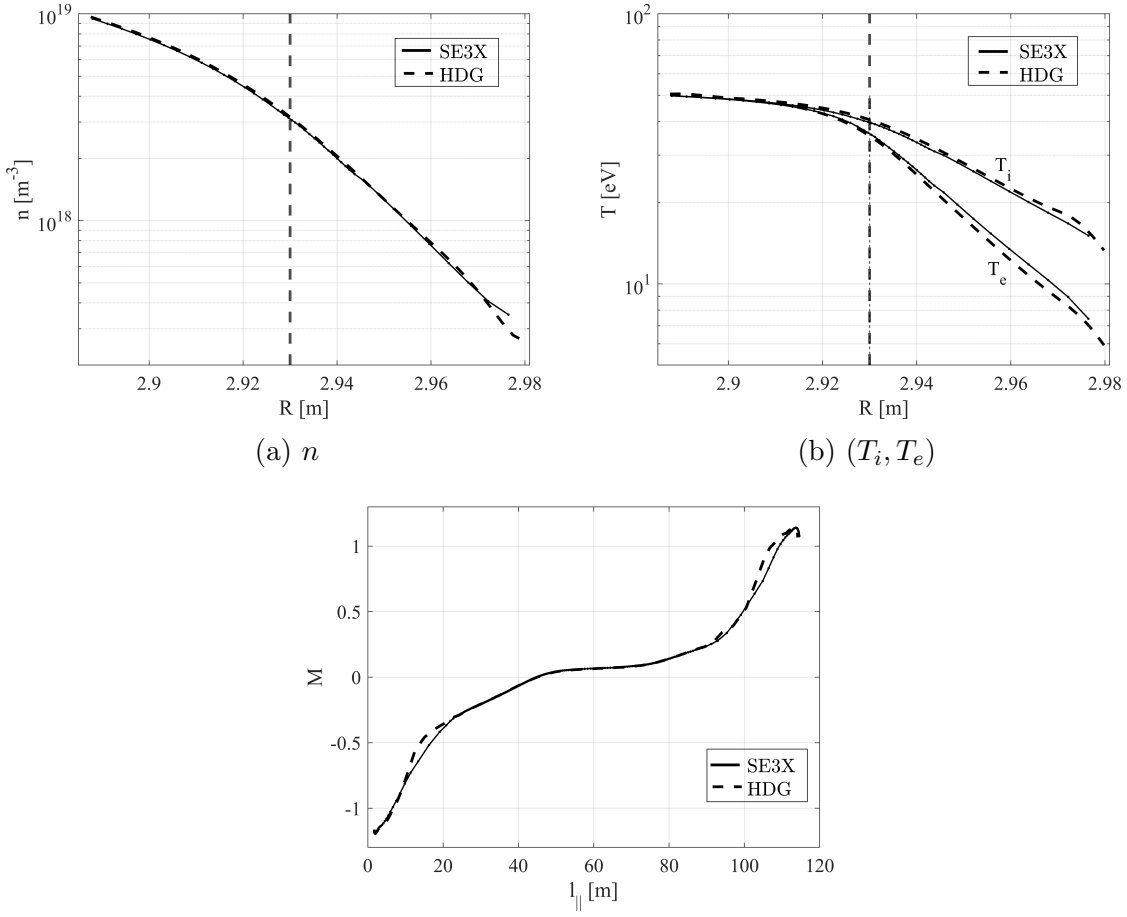

(a) n (b) (T_i, T_e)

(c) M

Figure 7: Comparison of profiles obtained with SolEdge3X (solid line), and SolEdge3X-HDG (dash line) in the WEST geometry. LFS mid-plane radial profiles of the density n (a) and the ion and electron temperatures (b). Parallel profiles of the parallel Mach number M along the separatrix (c).$l_{\|} = 0$ corresponds to the outer divertor target.

which is aligned or non aligned with the magnetic field depending on the method. In the first case, the Bohm boundary conditions can be prescribed at the wall imposing an outgoing flux of particles and energy while in the second case the immersed boundary method leads unavoidably to a thin grey zone in the near wall region. The agreement on the parallel Mach number profiles is also good, Fig. 7c. In particular, the parallel Mach number values at the the divertor plates are the same, showing that boundary conditions in the parallel direction leads to the same flow conditions. The main difference between the profiles is visible around the X-points locations which could be expected due to the discretizations used in the two codes and the issue to keep the alignment in presence of a singularity with SolEdge3X.

Regarding now the e-folding lengths, we find comparable values to that of the circular limiter simulations given above with $\lambda_n = 2.10^{-2}m$, $\lambda_{T_e} = 3.10^{-2}m$ and $\lambda_{T_i} = 5.10^{-2}m$, Figs. 7a, b. The main difference is found for the density profiles which

exhibits opposite curvatures at this LFS location. This effect is mostly likely related to the observed parallel variation of the parallel Mach number M Fig. 7c. Besides the transition to the supersonic flows at the X-point in the absence of divertor ionization source one can notice that the variation of the Mach number is similar to $1/(1-M^2)$ prior to the X-point with a slight asymmetry governed by a shift of the stagnation point to the LFS.

In conclusion, the very good agreement obtained between the solutions makes us very confident on the capability of this new solver to predict numerical solutions in realistic configurations showing all the characteristics expected from the implemented physical model.

5. Simulation of an entire plasma discharge in WEST

The magnetic equilibrium free approach developed in this work allows us for the first time to simulate 2D fluid transport during an entire plasma discharge in WEST. We have chosen the shot #54487 which is a pure ohmic discharge. This discharge corresponds to a single null lower divertor configuration with a secondary separatrix with X point just outside the plasma at the top of the plasma volume.

5.1. Numerical setup

To carry out the simulation of the full WEST discharge #54487 presented in this work, the plasma equilibrium has been computed at 403 different times with a time interval equal to $dt = 0.02\ s$. The code needed 240 hours only on 32 cpus to reproduce the entire discharge that represents about 9 s of real time showing the efficiency of the numerical solver to simulate such kind of plasma evolution.

5.1.1. Configuration and mesh The geometrical configuration as well as the unstructured mesh are shown on Fig. 8. The mesh is composed by 26830 p=4 elements discretizing the whole poloidal cross-section.

5.1.2. Boundary conditions The domain of computation is the whole tokamak cross-section, and thus only boundary conditions at the plasma facing components are needed. The standard Bohm boundary conditions are applied for the velocity (Eq. 5) as well as for the ion and electron energies (Eq. 6). Plasma recycling takes into account the flux of neutrals (Eq. 9). The recycling coefficient R, which governs with D_n the total quantity of matter in the system, is fixed to 0.998.

5.1.3. Control parameters The values assigned to the perpendicular transport coefficients for the plasma and for the isotropic diffusion for neutrals are chosen in function of experimental measurements and to match as accurately as possible with the lines integrated density values measured by the interferometry. The transport

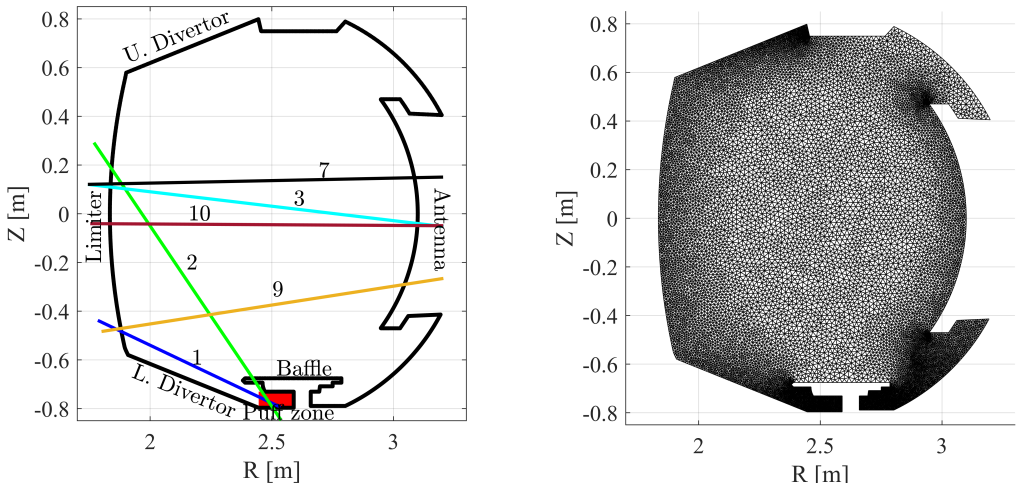

Figure 8: WEST configuration (a) and unstructured mesh (b). The tokamak plasma facing components are labeled as the upper divertor, the left limiter, the lower divertor, the baffle and the antenna. The red rectangle under the baffle denotes the location of the gas puff source. The colored lines denote the traces of the interferometry lines of sight considered for comparisons with experiments.

coefficients for plasma are taken all equal to $D = \mu = \chi_i = \chi_e = 0.5\ m^2/s$ while the neutral diffusion is settled to $D_{n_n} = 2000\ m^2/s$. In order to mimic experimental gas puff injection, a time-dependent source term for neutral density has been implemented in the bottom right part of the machine under the baffle. For this case, the source is volumetric and homogeneous in the pumping plenum as shown in Fig. 8a.

5.1.4. Time dependent magnetic equilibrium, plasma current, and gas puff The plasma discharge #54487 in WEST is characterized by 4 different phases: the start-up including the limiter phase of the current ramp ($0 < t \leq 0.5s$), the ramp-up corresponding to a divertor phase with a fast linear plasma current increase ($0.5 < t \leq 2s$), the flat-top steady state ($2 < t \leq 6.7s$) and the ramp down until plasma termination ($6.7 < t \leq 9s$), as shown on Figs. 9 and 10. The time evolution of the magnetic equilibrium and the corresponding plasma current as well as the gas puff rate are extracted from the WEST experimental database. The magnetic equilibrium is interpolated on the grid nodes and smooth in time to avoid any spurious behavior governed by the reconstruction. The plasma current density evolution Fig.10a is used to calculate self-consistently the energy source from the ohmic heating. Concerning the gas puff rate Fig. 10b, the circles represent the values implemented in the code at different time steps, while the peak before $t = 0$ corresponds to the prefill of the machine with neutral gas before the beginning of the experimental discharge.

5.1.5. Simulation setup At $t = 0$, the code is run in a steady mode using the first magnetic equilibrium and corresponding current density distributions to calculate the initial condition. The initial value of the total density $n_{tot,0}$ is the integral in time of the gas puff rate prior to the beginning of the discharge at $t = 0\ s$, and divided by the volume of machine, Fig. 10b. This value quantifies the total amount of matter in the machine. The value of the puff rate is not defined at $t = 0\ s$, and so it is tuned in order to have a total amount of matter equal to the reference value $n_{tot,0}$.

At each following time step, the corresponding magnetic equilibrium, the related current distribution to compute the ohmic heating, and the value of the gas puff rate (Fig. 10) are loaded, and the code is run over 0.02s, which is much smaller than the time would be needed to get convergence as demonstrated below (Eq.13). Then, it is advanced in time, loading the new values of plasma current and gas puff as well as the new magnetic equilibrium. Thus the time step of the code is set equal to the time difference between two successive experimental acquisitions. The implicit time integration removes any constraint of stability on the time step value, but sometimes it has to be reduced to deal with significant and fast changes in the magnetic equilibrium that could lead to a computation blow up.

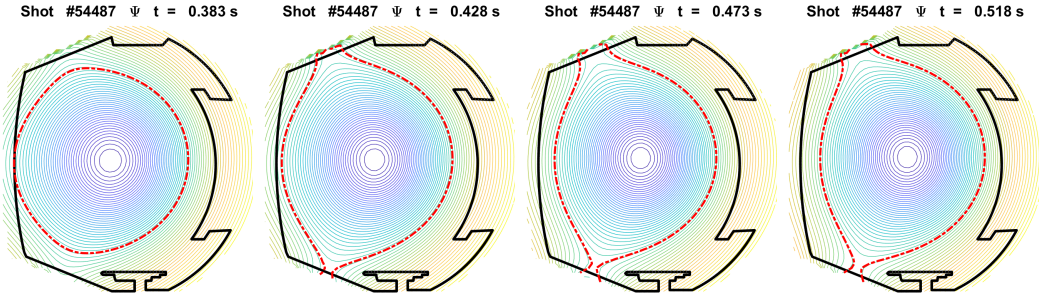

(a) Limiter-Divertor transition

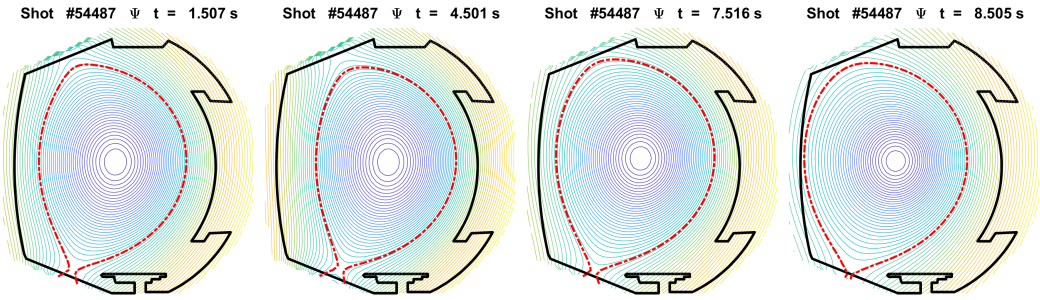

(b) Ramp-up (c) Flat-top (d) ramp-down

Figure 9: Time evolution of the magnetic equilibrium (the red dashed line is a proxy for the separatrix) in different phases of the discharge denoted in 10a: Limiter divertor transition start-up ($0 < t \leq 0.5\ s$) (a), ramp-up ($0.5 < t \leq 2\ s$)(b), flat-top ($2 < t \leq 6.7\ s$) (c) and ramp down ($6.7 < t \leq 9\ s$)(d).

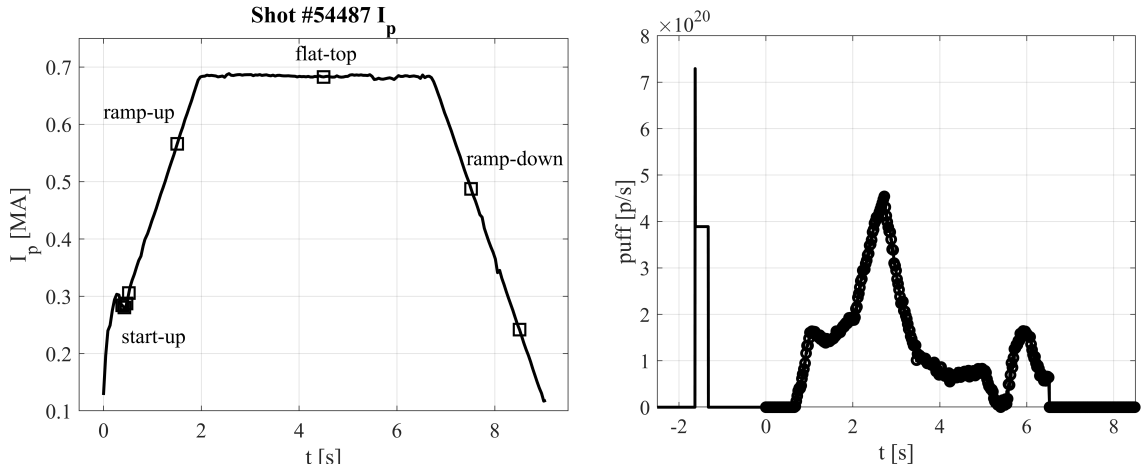

(a) (b)

Figure 10: Time evolution of the total plasma current (a) and of the gas puff rate (b) extracted from the experimental WEST shot #54487. The black squares in (a) denote the temporal position of plots in Fig. 9. In (b), the circle points show the value used by the code and the solid line denotes the refueling of the machine with neutral gas before the beginning of the experimental discharge. The time integral of the trace line before the time 0 measures the total amount of matter inserted in the machine. L-D transition start-up ($0 < t \leq 0.5s$), ramp-up ($0.5 < t \leq 2s$), flat-top ($2 < t \leq 6.7s$) and ramp down ($6.7 < t \leq 9s$).

5.2. Plasma evolution during the discharge

The solution is analyzed during the four steps of the discharge corresponding to the start-up (limiter divertor transition), the ramp-up (plasma current increase), the flat-top (steady state) and the ramp-down (plasma current decrease until plasma termination).

5.2.1. L-D transition during the start-up phase ($0 < t \leq 0.5$ s) The evolution of the plasma equilibrium during the start-up of the WEST discharge #54487 is shown on Fig. 11. At the very beginning of the discharge the plasma has a circular shape, intersecting the tokamak inner wall in a limiter configuration. Progressively, the separatrix (the red dashed line depicted in Fig. 9a) enters into the domain moving to the LFS with the X-point localized outside of the plasma volume. Finally the separatrix further shrinks into the plasma volume and the lower X-point moves up to generate the characteristic divertor configuration from $t = 0.428$ s to $t = 0.473$ s.

All plasma quantities follow the evolution of the magnetic equilibrium, and take constant values along the magnetic surfaces as shown at the beginning of the discharge during the limiter-divertor transition. During this transient with constant particle diffusion, the steady state density profile is not reached and the density profile is not flat in the core region where the particle source is negligeable. Indeed the particle diffusion time from the tokamak edge, where the sources are located (recycling of the plasma at the wall or gas puff after ionization), to the core, is larger than the duration of the transient phase between two magnetic equilibriums. In the present simulations, with a

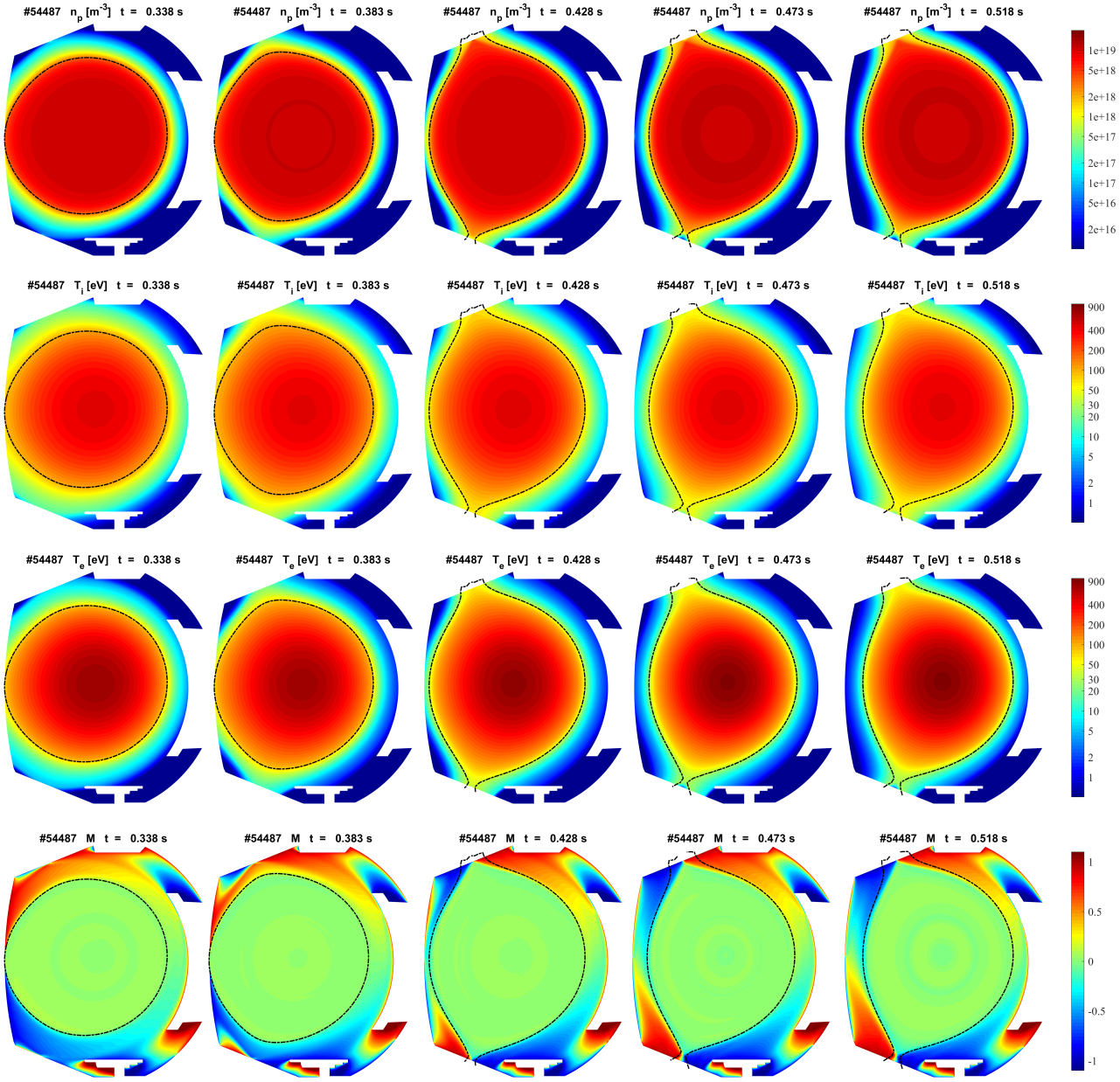

Figure 11: Snapshots of the plasma density (1st row), ion temperature (2nd row), electron temperature (3rd row), and Mach number (4th row) at 5 time steps during the limiter-divertor transition of the experimental WEST shot #54487.

minor radius of the machine equal to $a = 0.5\ m$ and with a perpendicular transport coefficient $D = 0.5\ m^2/s$, the time to diffuse to the center of the machine is equal to about $0.5\ s$ while the time of the transient phase is of the order of the time step of the simulation $dt = 0.02\ s$. An additional effect can be related to the background noise or error of measurements in the data of the magnetic equilibrium. The snapshots also show that the electron temperature in the core is higher than the ion temperature. A more quantitative comparison on the profiles shows that $T_e \approx 2T_i$. This is related to the ohmic heating, which only heats the electrons and to the reduced efficiency of

collisional temperature equipartition compared to the turbulent cross-field transport. At the beginning of the discharge the plasma collisionality is particularly weak given the high temperatures and low densities. Finally, regarding now the parallel Mach number maps, the angle of incidence of the magnetic field lines with the wall changing during the start-up, the sign of the Mach number also changes on the HFS.

5.2.2. Solution during the flat-top phase ($2 < t \leq 6.7\ s$) The solution obtained during the flat-top phase is analyzed here at $t = 4.510\ s$. Fig. 12 shows the 2D map for the plasma density, the ion and electron temperature, the parallel Mach number as well as the neutral density. During the ramp-up phase, the gas puff rate is feed backed to increase up to the core value, $\approx 5e19\ m^{-3}$. Due to the low power injected, a peak of density appears at the X-point, which plays the role of a stagnation point, and it extends towards the core region crossing the separatrix. For such values the mechanism of energy exchange becomes more efficient, and the ion and electron temperatures thermalize towards the same value. However, the high electron temperature in the core doesn't allow a perfect equipartition of the energy between the two species (ions and electrons), and T_e values are $\approx 80\ eV$ higher than T_i values.

The steady state solution during the flat-top phase of the discharge is the one usually investigated by the 2D fluid transport codes without taking into account the transient phase obtained since the beginning of the discharge. To emphasize the impact of the transient on the prediction of the plasma quantities, another simulation has been performed from scratch (manufactured initial condition), using the fixed plasma equilibrium of Fig. 9c and the respective plasma current and gas puff rate values measured at $t = 4.510\ s$. In this computation, the steady-state version of the algorithm is used and the time derivatives of Eqs. 1-4, 7 are off.

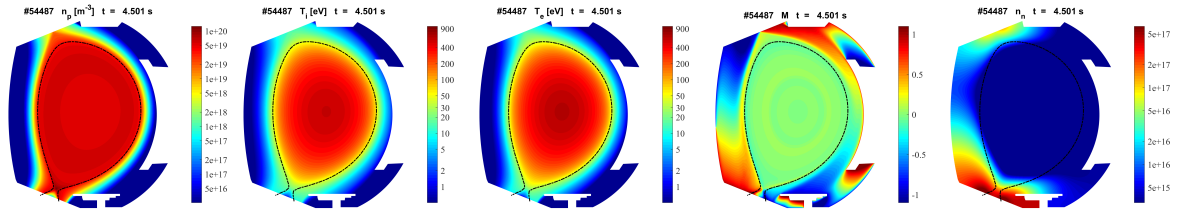

(a) n (b) T_i (c) T_e (d) M (e) n_n

Figure 12: 2D maps of the plasma quantities at $t = 4.510\ s$ during the flat-top phase incorporating the transient phase (unsteady computation) of the WEST shot #54487.

The relative differences, $\frac{\delta n}{\overline{n}}$, $\frac{\delta T_i}{\overline{T_i}}$, $\frac{\delta T_e}{\overline{T_e}}$ and $\frac{\delta n_n}{\overline{n_n}}$, between the solution integrating the transient phase (Fig. 12) and the steady solution computed from scratch are shown at the LFS mid-plane on Fig. 13. For plasma density, the difference is positive everywhere along the radius, and increases around the separatrix. Thus, the density values are higher in the unsteady computation than in the steady one. This means also that the system looses less matter and that the system doesn't reach the stationary state over

the time scale of the time step between two magnetic equilibriums. In order to show this, we compute the time variation of the number of particles at one instant during the flat-top phase. The computation is done at $t = 4.510$ where the steady calculation has been performed (see on Fig. 13) :

$$\frac{\int_\Omega \partial_t n dv}{\int_\Omega n dv}|_{t=4.51} = -3.15 \times 10^{-4} s^{-1} \tag{13}$$

where Ω is the volume of the computational domain. This means that the total number of particle $N = \int_\Omega n dv$ decreases in time during the flat-top phase, that agrees with the results plotted on Fig. 13. The absolute value of this result is the inverse of a characteristic time equal to $\tau = 3 \times 10^4\ s$, which gives an estimate of the time needed to reach the stationary state. Indeed, the following equation for the conservation of the total number of particles with a constant rate of gas injection Q_{puff} $[ps^{-1}]$ (like for usual steady state simulation):

$$\frac{\partial N}{\partial t} = \frac{N}{\tau} + Q_{puff} \tag{14}$$

leads to the solution:

$$N(t) = Q_{puff}\tau(1 - e^{-t/\tau}) + N_0 e^{-t/\tau} \tag{15}$$

where N_0 is the initial total number of particle. This result shows that the total number of particle relaxes to $Q_{puff} \times \tau$ above a characteristic time scale of the order of τ, which is much larger than $dt = 0.02s$ which is the time step between two magnetic equilibriums. The largest difference appears in the SOL just in the vicinity of the separatrix, highlighting the role of the time in the particle diffusion from sources related to the recycling at the wall. As a consequence of a smaller plasma density in the steady computation, both temperatures are larger in the core ($\delta T_{i,e}/\overline{T}_{i,e} < 0$ for $R < 0$) than in the unsteady solution. However, due to the thermalization effect in the SOL the temperature difference changes of sign in this plasma region.

Also Fig. 13c shows that neutral density is higher in the unsteady computation than in the steady one. That confirms an improved conservation of matter when the transient phase is accounted. The peak is reached in the core, where due to lower temperatures, the ionization cross-section decreases reducing the rate of ionization for neutral particles. Let's notice that the oscillations in the n, T_i and T_e profiles are related to the background noise in the magnetic equilibrium measurements. Conversely, the absolute neutral density being independent of the experimental magnetic equilibrium its profile is smooth.

5.2.3. Solution evolution during the ramp down ($6.7 < t \leq 9s$*)* In the last phase of the discharge the plasma current decreases until plasma termination. During this phase the closed magnetic surfaces move back to the HFS, as shown by the dashed red line of Fig. 9d, and switch back to a limiter configuration. The solution at $t = 8.505\ s$ is shown on Fig.14.

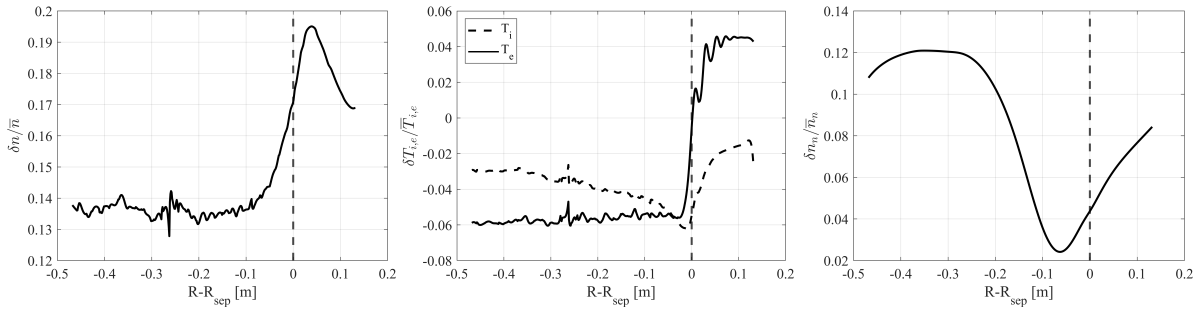

(a) (b) (c)

Figure 13: Relative difference at the LFS mid-plane between solutions computed with transient phase and not for plasma density $\frac{\delta n}{\overline{n}}$ (a), ion and electron temperatures ($\frac{\delta T_i}{\overline{T_i}}$, $\frac{\delta T_e}{\overline{T_e}}$) (b) and neutral density $\frac{\delta n_n}{\overline{n_n}}$ (c). ($\bar{\cdot}$) is the arithmetic average between the two solutions. The reference time is $t = 4.510\ s$ and the dashed line denotes the separatrix position.

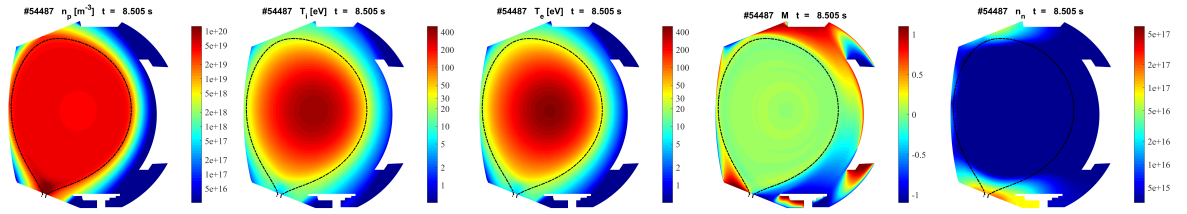

(a) n (b) T_i (c) T_e (d) M (e) n_n

Figure 14: 2D maps of the plasma quantities at $t = 8.505\ s$ during the ramp-down phase of the WEST shot #54487.

5.3. Comparison with experimental interferometry data during the discharge

The interferometry diagnostic in WEST allows a more quantitative comparison of the plasma density evolution during the discharge. Numerical and experimental results are compared over time using the lines of sight defined in Fig. 8a in the core region and at the edge and around the X-point, Fig. 15a, b respectively. A global qualitative agreement can be observed on the density. Numerical profiles even show a more quantitative matching with the experimental data in the central region on lines 3, 7 and 10, particularly during the flat-top phase. Moreover, even if the numerical values are smaller than the experimental ones, the simulations predict relatively well the increase during the ramp up (Fig. 15a). In the edge (Fig. 15b), the simulations tend to overpredict the experimental level with a maximum of about 50%, the largest difference being along the line 2, located between the baffle and the limiter. One can also notice that some profiles transient variations in time are also recovered by the simulation.

The density profiles are more peaked in the center in experiments than in the simulations, where the profile appears to be flatter. This can be again related to the particles sources located at the wall in our model (recycling and gas puff after ionization), and a cross-field turbulent transport which is only diffusive. Inward pinch velocities

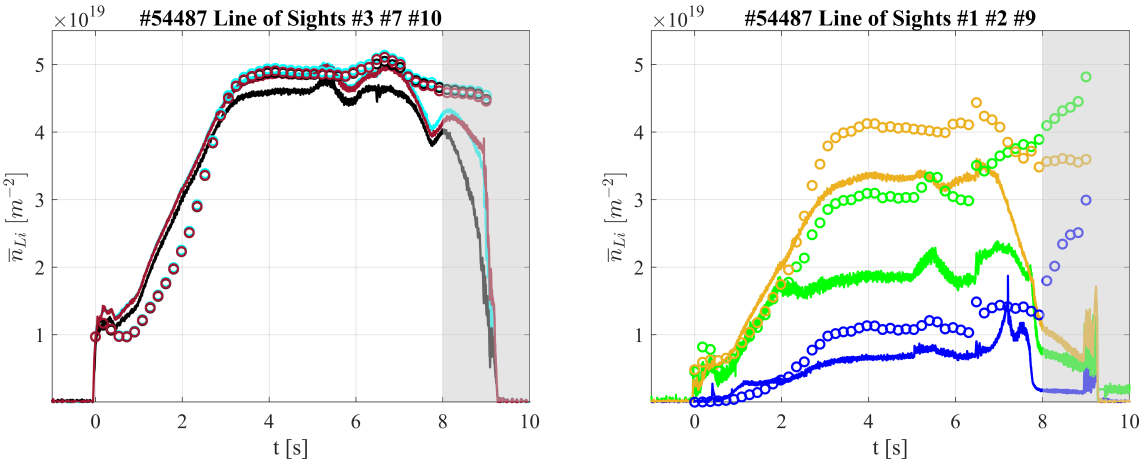

(a) Central (3,7,10) line integrated density (b) Edge (1,2,9) line integrated density

Figure 15: Comparisons of the temporal traces of experimental interferometry data (continuous line) and numerical data (circle) for different lines of sights defined in Fig. 8a: 3, 7, 10 for the centre (a) and 1, 2, 9 for the edge (b).

should be considered to yield peaked core profiles.

This difference between numerical and experimental data could be caused by the high recycling coefficient $R = 0.998$ needed in the present simulations to reach the right density in the center of the machine. The transport of particles in the perpendicular direction being purely diffusive, a high quantity of matter is needed to push plasma particles to enter and fill up the core region. As a consequence, it is possible that the total quantity of matter is slightly overestimated leading to the mismatch observed in Fig. 15b. Further more, the model for neutrals is simply diffusive with an isotropic diffusion coefficient. This is a strong limitation in the case the density is too low to be treated in a collisional framework. In such conditions the neutral dynamics should be more ballistic than diffusive, that would impact on the location of the source of ionization and consequently the plasma density and hence the line integrated density.

Finally, the two plots clearly show that numerical data are not able to predict the last seconds of the discharge (ramp-down) both at the center and at the edge.

5.4. Time evolution of the plasma quantities at the PFCs

The time evolution of the plasma quantities at the PFCs (Figs. 16, 17) provides critical information for the operation. The use here of an unstructured mesh allows an accurate discretization of all the plasma facing components and thus makes us confident on the plasma quantities values obtained in the frame of the resolved physical model.

At the beginning of the discharge ($t < 1$ s), the heat and particle fluxes are concentrated on the HFS limiter. The configuration switches to the X-point at ($t = 0.5$ s) and the maximum of the fluxes move toward the upper and lower divertor. As shown in the first row of Fig. 16, the peaks of fluxes normal to the wall are reached

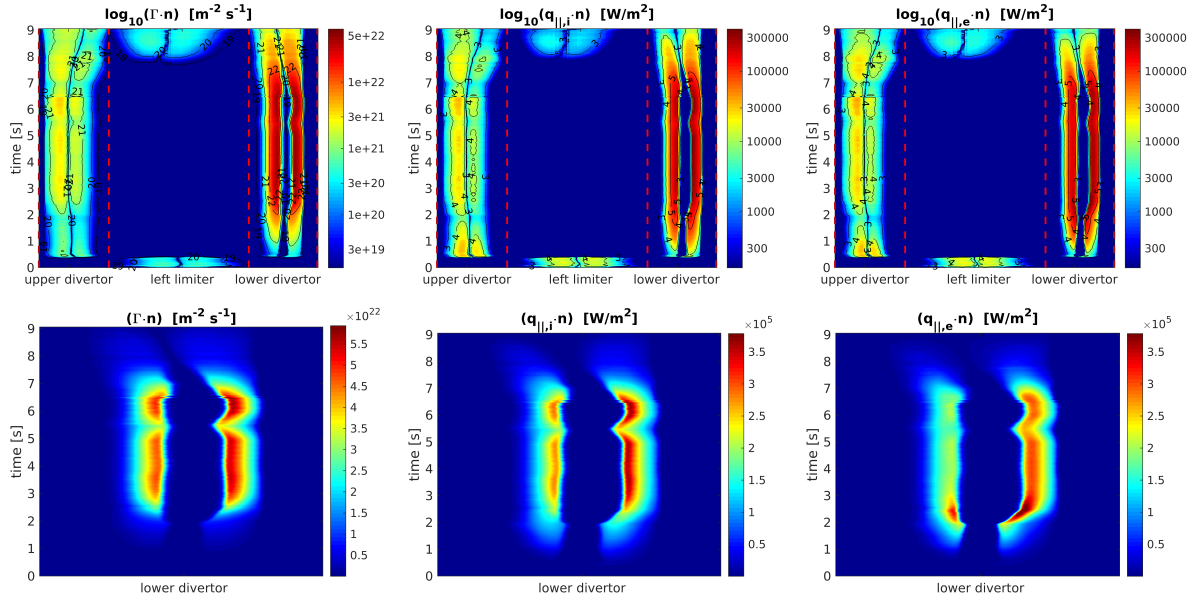

(a) (b) (c)

Figure 16: Spatio-temporal diagram of the particle flux (a), the ion (b) and electron (c) heat fluxes projected in the direction normal to the wall, in function of the wall coordinates (horizontal-axis) and time (vertical-axis). In the first row, the results are plotted in log scale along all the PFCs (upper divertor, left limiter and lower divertor according to Fig. 8a). In the second, results are zoomed on the lower divertor using a linear scale.

at the lower divertor with a magnitude about one order larger than at the upper divertor and left limiter position. On the lower divertor, the maxima for particle and heat loads are located at the outer target, mostly due to the fact the confinement is stronger at the high field side and that the perpendicular transport (constant everywhere in the current model) is thus less effective. However, the location of the peaks is non constant in time, and spreads along the lower divertor coordinates. Also if at the onset of the X-point the electron heat flux is dominant, the ion heat flux becomes dominant during the stationary phase of the discharge.

Fig. 17 shows the spatio temporal diagram for T_i, T_e and their ratio $\tau = T_i/T_e$ which provides an information on the energy equipartition. At the beginning of the discharge ($t < 1\ s$) the plasma temperatures are high at the limiter surface then at the upper and lower divertor when X-point occurs, with a maximum value around 80 eV. Then the temperatures decrease to $\approx 10\ eV$ in the stationary phase. $\tau = T_i/T_e$ varies in space and time, Fig. 17 c, d . On the antenna and the baffle T_i is globally $2-3$ times larger than T_e. At the lower divertor (Fig. 17 c) τ is changing in time, with values that can be smaller than 1 during the ramp up ($t < 2\ s$) at some locations at the plate, and that increase above 1 almost everywhere during the flat top phase. The trend is opposite at the secondary divertor with values that can be smaller than 1 around the middle of the plate during the steady phase $t > 2\ s$.

To show the potential attractiveness of the current numerical approach for fusion

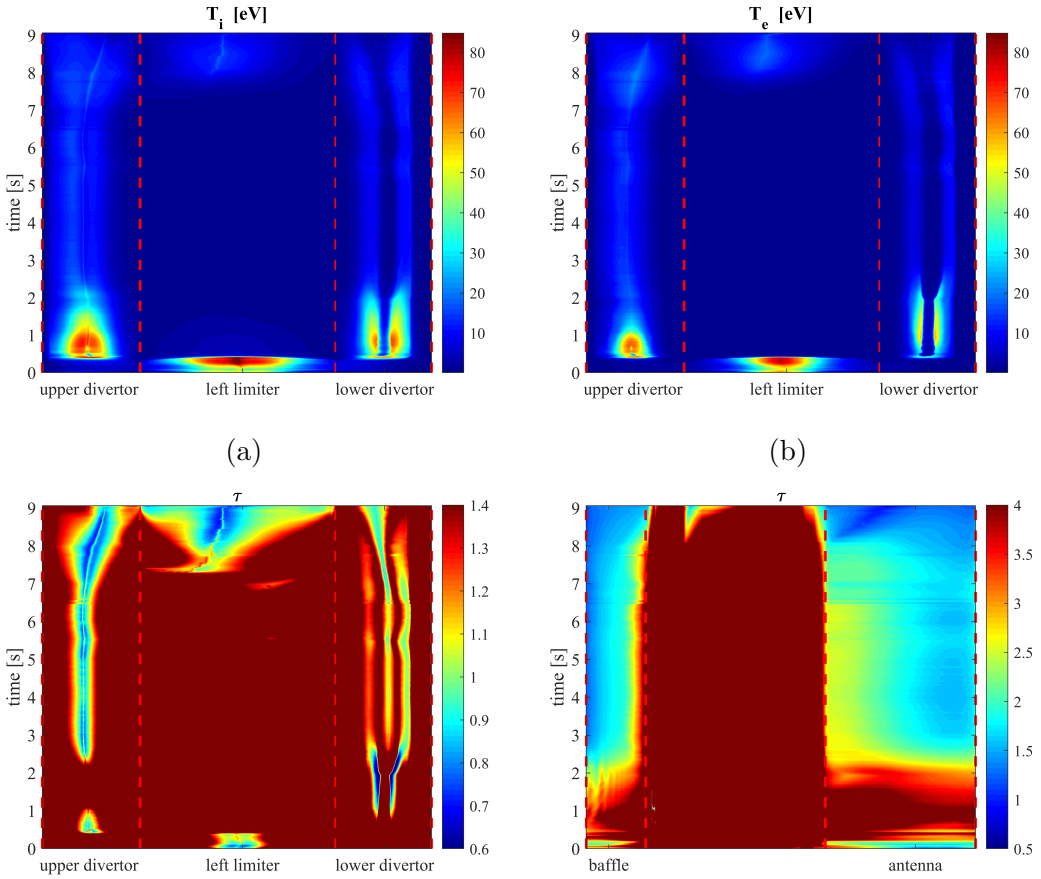

Figure 17: Spatio-temporal diagram of the ion (a) and electron (b) temperature, and of their ratio $\tau = T_i/T_e$ (c, d) in function of the wall coordinate as indicated in Fig. 8a.

operation, we finally address the $D^+ - W$ contribution to erosion using a crude model inspired by [23]. The effective W sputtering is a complex function of the plasma parameters at the PFCs. We however assume here that the W-sputtering is directly related to a threshold value of the energy of impact and we do not take into account the large fraction of emitted W that can return back to the PFCs. This threshold value of the energy of impact is estimated from a kinematic treatment of the energy and momentum balance at $E_{th} = 220\ eV$ to release a W atom in a head-on D-W collision [23]. For an ion after crossing the sheath, E_{impact} is approximated by $2k_bT_i + Z3k_bT_e$, Z being the ion charge state. Knowing the spatio-temporal distribution of T_e and T_i during the discharge, we evaluate the tungsten influx Γ_W and the total tungsten contamination over the time of the disharge W_{ToT} defined as

$$(a)\ \ \Gamma_W(\boldsymbol{x},t) = \mathcal{H}(E_{impact} > E_{th})\Gamma_{D^+} \qquad (b)\ \ W_{ToT}(t) = \int_{\partial\Omega} \mathcal{H}(E_{impact} > E_{th})\Gamma_{D^+} ds \tag{16}$$

where $\mathcal{H}$ is the Heaviside function, and $\partial\Omega$ is the surface of the tokamak wall. Γ_W is

estimated assuming that a D^+ ion impacting the wall with an energy larger than E_{th} takes away a W atom from the wall. Fig. 18 makes a zoom over the start-up and the ramp-up phases related to the evolution of these two quantities. Based on this model, our analysis show that the W-sputtering mainly occurs at the beginning of the discharge since after $t = 1.5\ s$ the plasma at the PFCs is too cold for the impact energy to be larger than the estimated threshold for sputtering. During the start up, the sputtering is localized at the limiter, and to a much lesser extent at the antenna. During the ramp-up phase, the peak of Γ_W is now localized on the lower divertor. At this stage the plasma is approaching the diverted configuration and the particles flux to the wall is still significant. The elongated shape in time of this structures suggests that the current ramp-up time of the plasma current (see Fig. 10a) and density (see Fig. 10b) is critical to determine the W contamination.

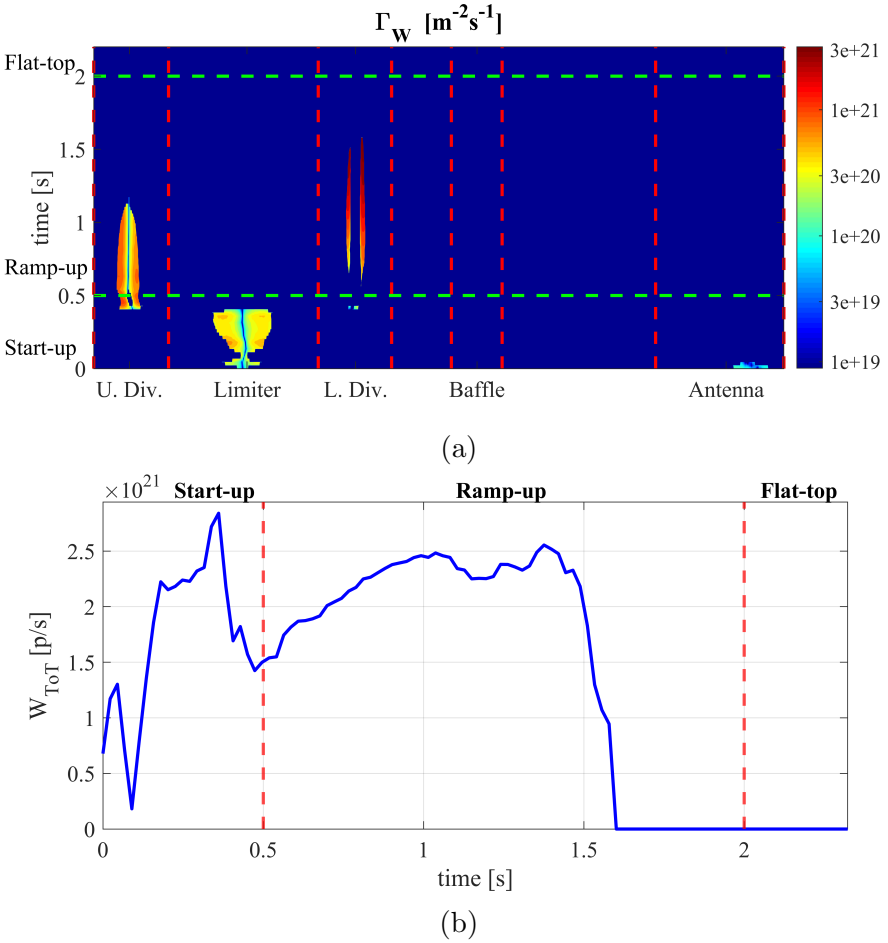

Figure 18: W-sputtering at the PFCs. (a) Spatio-temporal distribution of the W influx estimated from Eq. 16. (b) Time evolution of the surface integrated W flux during the discharge.

The time evolution of the surface integrated flux of tungsten (Fig. 18b) provides a more quantitative information. The totality of the surface integrated flux of tungsten is injected into the plasma before the end of the ramp-up phase ($t \approx 1.6\ s$). More

precisely, its maximum value is reached during the start-up around $t = 0.4\ s$, with a value of about 12% larger than in the peak value reached during the ramp-up phase. At this time, the plasma is still in the HFS limiter configuration but the upper and lower X-points are moving out of the wall.

6. Conclusion

This work reports the first 2D transport fluid simulations in the entire poloidal cross-section of WEST during a full discharge including the four phases: the start-up including the limiter phase of the current ramp and the limiter-divertor transition, the ramp-up corresponding to a divertor phase with a fast linear plasma current increase, the flat-top steady state and the ramp down until plasma termination. The physical model, based on 2D Braginskii fluid equations has been enriched by self-consistent sources of matter and energy. The model for neutrals dynamics is purely diffusive. The energy source is provided by ohmic heating as in the experimental discharge. The magnetic equilibrium, plasma current and gas-puff rate evolution are determined according to the experimental data base (WEST shot #54487). This kind of simulation is made possible for the first time through the use the new high-order finite elements method recently developed [14–16]. Unlike conventional approaches, the unstructured mesh is independent of magnetic equilibrium, and the high order approximation scheme guarantees low digital dissipation despite the misalignment with the magnetic equilibrium.

The results show the evolution during the whole discharge of all relevant plasma quantities together with the magnetic equilibrium, e.g. density prole, electron and ion temperatures. If at the onset of the X-points during the ramp-up the electron heat ux is dominant at the target, present results show that the ion heat ux becomes dominant during the stationary phase of the discharge. Comparisons with the interferometry diagnostic show that the model with the well-tuned values of the control parameters, and particularly of the recycling coefficient, is able to provide solutions in a remarkable overall qualitative agreement with experiment during the discharge. The agreement can be even quantitative at some locations in the plasma core. However, comparisons with experimental temperatures profiles, if available, would probably have led to larger differences due to missing impurities radiation in the energies balance.

Moreover, interpreted using a simple theoretical model for erosion, present results assess the tungsten sputtering due to deuterium ions mainly occurs during the start-up and the ramp-up phase of the discharge, usually not taken into account in current 2D transport simulations. These results seem to confirm the role of the limiter divertor transition for the tungsten contamination which remains a critical issue for fusion operation in machine like ITER as the plasma current is built-up. Indeed, the W radiations can then modify this current profile, and generate low performance scenario plagued by MHD relaxations. Moreover, according to the theoretical model used here, in case of light impurities, like O and C, or even Be, much lower temperatures $\approx 10-20\ eV$ are sufficient to trigger W sputtering making the impact of W radiation on performance

even more critical. This remains for a future work since even if dedicated models already exist to address the impact of light impurities in term of W contamination ([30, 31]) they neglect the transient phase preceding the flat-top phase, and thus the the strong limiter erosion during that phase.

The comparison between the solutions obtained in a steady mode, as usually performed in current simulations of the literature, and in the unsteady mode taking into account the evolution of the magnetic equilibrium, the plasma current and of the gas-puff rate evolution since the beginning of the discharge show significant differences in particular on the plasma density in the core (+14% in the unsteady mode) and in the SOL (up to + 20%).

These results are very encouraging, and show the need to consider full discharge simulations to support experimental data analysis and to target predictive capabilities in the future. The magnetic equilibrium free solver and the efficient time integration scheme of Soledge3X-HDG solver seem to be suitable to provide reliable simulations in this context.

Acknowledgement

This work has been carried out within the framework of the EUROfusion Consortium and has received funding from the Euratom research and training programme 2014-2018 and 2019-2020 under grant agreement No 633053. The views and opinions expressed herein do not necessarily reflect those of the European Commission. This work has been carried out thanks to the support of the A*MIDEX project (ANR-11-IDEX-0001 02, TOP project) funded by the 'Investissements d'Avenir' French Government program, managed by the French National Research Agency (ANR). This work has been also supported by the French National Research Agency grant SISTEM (ANR-19-CE46-0005-03). This work was granted access to the HPC resources of IDRIS under the allocations A0030506912 & A0050506912 made by GENCI, of Aix-Marseille University, financed by the project Equip@Meso (ANR-10-EQPX-29 01), and of the EUROfusion High Performance Computer (Marconi-Fusion) under the project HEAT.

Appendix A. Expressions of the ionization recombination-radiation terms

$$
\begin{aligned}
&S_{n,iz} = -S_{n_n,iz} \qquad S_{n,rec} = -S_{n_n,rec} \\
&S_{\Gamma,cx} = -n_n n u < \sigma v >_{cx} \quad S_{\Gamma,rec} = -n^2 u < \sigma v >_{rec} \\
&S_{E_i,iz} = n_n n < \sigma v >_{iz} \left[\frac{1}{2} m_i u^2 + \frac{3}{2} k_b T_i\right] R_E \quad S_{E_i,rec} = -n^2 < \sigma v >_{rec} \left[\frac{1}{2} m_i u^2 + \frac{3}{2} k_b T_i\right] \\
&S_{E_i,cx} = -n_n n m_i u^2 < \sigma v >_{cx} \quad R_E = 0.2 \\
&S_{E_e,iz} = -n_n n < \sigma v >_{iz} k_b T_{loss} \quad S_{E_e,rec} = -n^2 < \sigma v >_{rec} k_b T_{loss,rec} \\
&T_{loss} = \left(25 + 170 \exp\left(-\frac{T_e}{2}\right)\right) \quad T_{loss,rec} = min\left(250, 8 \exp\left(\frac{T_e}{9}\right)\right) \quad [eV]
\end{aligned}
\tag{A.1}
$$

$< \sigma v >_{rec}$ is the recombination cross section rate [26]. R_E is a free parameter to quantify the energy exchange in a ion-neutral collision since in the current model there is no energy equation for neutrals. Here, we assume that 20% ($R_E = 0.2$) of the neutral energy is transferred to the ion. T_{loss} and $T_{loss,rec}$ are adhoc expressions that quantify the electron energy radiative losses. In most regimes they play a minor role.

Appendix B. Conservative variables and system of equations

Eqs. 1-4 are recast in a conservative form. Introducing the vector $\boldsymbol{U} = \{U_1, U_2, U_3, U_4\}^T = \{n, nu, nE_i, nE_e\}^T$ (the superscript T stands for transpose), and the new unknown $\boldsymbol{Q} = \boldsymbol{\nabla U}$ Eqs. 1-4 become:

$$\begin{cases} \boldsymbol{Q} - \boldsymbol{\nabla U} = 0 \\ \partial_t \boldsymbol{U} + \boldsymbol{\nabla} \cdot (\boldsymbol{F} - D_f \boldsymbol{Q} + D_f \boldsymbol{Q} \boldsymbol{b} \otimes \boldsymbol{b} - \boldsymbol{F_t}) + \boldsymbol{f}_{E_{||}} + \boldsymbol{f}_{EX} - \boldsymbol{g} = \boldsymbol{s} \end{cases} \tag{B.1}$$

where $\boldsymbol{f}_{E_{||}} = \frac{2}{3}\boldsymbol{\nabla} U_4 \frac{U_2}{U_1} \cdot \boldsymbol{b}\{0,0,1,-1\}^T$, $\boldsymbol{F}_{EX} = \frac{1}{\tau_{ie}} \left(\frac{2}{3M_{ref}}\right)^{-1/2} \frac{U_1^{5/2}}{U_4^{3/2}} \left(U_3 - U_4 + \frac{1}{2}\frac{U_2^2}{U_1}\right) \cdot \{0,0,1,-1\}^T$, $\boldsymbol{g} = \{0, \frac{2}{3}\left(U_3 + U_4 - \frac{1}{2}\frac{U_2^2}{U_1}\right)\boldsymbol{\nabla \cdot b}, 0, 0\}^T$, $\boldsymbol{s} = \{S_n, S_\Gamma, S_{E_i}, S_{E_e}\}^T$. M_{ref} is a dimensionless parameter that appears by making the equations dimensionless, its value is $M_{ref} = \frac{T_0 e}{m_i u_0^2} \approx 12.5$, where e is the electron charge ($1.6e^{-19}$ C), m_i is the ion mass ($3.35e^{-27}$ kg), T_0 and u_0 are the reference temperature and velocity (50 eV and 1.3839 ms^{-1} respectively).

The diffusion tensor D_f is defined as:

$$D_f = \begin{bmatrix} D & 0 & 0 & 0 \\ 0 & \mu & 0 & 0 \\ 0 & 0 & \chi_i & 0 \\ 0 & 0 & 0 & \chi_e \end{bmatrix}$$

while the convective flux tensor $\boldsymbol{F(U)}$ is:

$$\boldsymbol{F} = \begin{Bmatrix} U_2 \\ \frac{U_2^2}{U_1} + \frac{2}{3}\left(U_3 + U_4 - \frac{1}{2}\frac{U_2^2}{U_1}\right) \\ \left(U_3 + \frac{2}{3}\left(U_3 - \frac{1}{2}\frac{U_2^2}{U_1}\right)\right)\frac{U_2}{U_1} \\ \left(U_4 + \frac{2}{3}U_4\right)\frac{U_2}{U_1} \end{Bmatrix} \otimes \boldsymbol{b^T}$$

Finally the parallel diffusion flux tensor is defined as:

$$\boldsymbol{F}_t = \begin{Bmatrix} 0 \\ 0 \\ k_{||i}\left(\frac{2}{3M_{ref}}\right)^{7/2}\left(\frac{U_3}{U_1 - \frac{1}{2}\frac{U_2^2}{U_1}}\right)^{5/2} \boldsymbol{Q^T V_i}(U)\cdot\boldsymbol{b} \\ k_{||e}\left(\frac{2}{3M_{ref}}\right)^{7/2}\left(\frac{U_4}{U_1}\right)^{5/2} \boldsymbol{Q^T V_e}(U)\cdot\boldsymbol{b} \end{Bmatrix} \otimes \boldsymbol{b^T}, \quad \boldsymbol{V_i}(U) = \begin{Bmatrix} \frac{U_2^2}{U_1^3} - \frac{U_3}{U_1^2} \\ -\frac{U_2}{U_1^2} \\ \frac{1}{U_1} \\ 0 \end{Bmatrix},$$

$$\boldsymbol{V_e}(U) = \begin{Bmatrix} -\frac{U_4}{U_1^2} \\ 0 \\ 0 \\ \frac{1}{U_1} \end{Bmatrix}$$

Appendix C. The HDG solver

The resolution of Eqs. B.1 is made through two steps [14].

In the first step a local problem is set and solved for each element of the discretization. The domain computation is divided in N_{el} disjoint elements with boundaries ∂K for $K = 1, ..., N_{el}$. The discontinuity setting induces a new problem with local element by element equations and some global ones. The introduction of new unknowns $\hat{\boldsymbol{U}}(\boldsymbol{x}, t)$, called traces solutions, restricted to skeleton of the mesh, is crucial for the second step of the HDG scheme, which allows to set up a global problem solving for $\hat{\boldsymbol{U}}$ in the whole mesh skeleton. In each element K the local problem corresponds to the plasma model Eq. B.1, with Dirichlet condition on the element boundary ∂K, which constrains $\boldsymbol{U}$ to be equal to $\hat{\boldsymbol{U}}(\boldsymbol{x}, t)$ for $\boldsymbol{x} \in \partial K$. Therefore given the values of $\hat{\boldsymbol{U}}$ on the element boundary, the Dirichlet condition imposed on the left and on the right element of a given face is the same, consequently the continuity of the unknowns is ensured.

In order to solve the local problem, the weak formulation of the system Eqs. B.1 is derived multiplying respectively the first two equations by a tensor test function $\boldsymbol{\mathcal{G}} \in \mathcal{P}^p$ and a vector test function $\boldsymbol{v} \in \mathcal{P}^p$, where $\mathcal{P}^p$ denotes the space of polynomial of degree less or equal to p. After integration by part, the resulting weak problem for each element corresponding to Eqs. B.1 becomes:

$$\begin{cases} (\boldsymbol{\mathcal{G}}, \boldsymbol{Q})_K + (\boldsymbol{\nabla \mathcal{G}}, \boldsymbol{U})_K - \left\langle \boldsymbol{\mathcal{G}} \boldsymbol{n}, \hat{\boldsymbol{U}} \right\rangle_{\partial K} = 0 \\ (\boldsymbol{v}, \partial_t \boldsymbol{U})_K - (\boldsymbol{\nabla v}, \boldsymbol{F} - D_f \boldsymbol{Q} + D_f \boldsymbol{Q} \boldsymbol{b} \otimes \boldsymbol{b} - \boldsymbol{F}_t)_K \\ + \left\langle \boldsymbol{v}, \left(\hat{\boldsymbol{F}} - D_f \hat{\boldsymbol{Q}} + D_f \hat{\boldsymbol{Q}} \boldsymbol{b} \otimes \boldsymbol{b} - \hat{\boldsymbol{F}}_t \right) \boldsymbol{n} \right\rangle_{\partial K} \\ + \left(\boldsymbol{v}, \boldsymbol{f}_{E_{||}} \right)_K + \left(\boldsymbol{v}, \boldsymbol{f}_{E_{EX}} \right)_K - (\boldsymbol{v}, \boldsymbol{g})_K = (\boldsymbol{v}, \boldsymbol{s})_K \end{cases} \tag{C.1}$$

In C.1 $\left(., .\right)_K$ denotes the $\mathcal{L}^2$ scalar product in the element K, while $\left\langle ., . \right\rangle$ denotes the scalar product of the traces in ∂K. The traces of $\boldsymbol{F}$ and $\boldsymbol{Q}$ on the element boundary have been replaced by numerical traces in this way:

$$\begin{aligned} \hat{\boldsymbol{F}}(\hat{U}) &= \boldsymbol{F}(\hat{U}) + \boldsymbol{\tau} \left(\boldsymbol{U} - \hat{\boldsymbol{U}} \right) \otimes \boldsymbol{n} \\ \hat{\boldsymbol{Q}} &= \boldsymbol{Q} \\ \hat{\boldsymbol{F}}_t(\hat{U}) &= \boldsymbol{F}_t(\hat{U}) \end{aligned}$$

where $\boldsymbol{n}$ is the outer normal to the element face and $\boldsymbol{\tau}$ is the local stabilization matrix. The definition of $\boldsymbol{\tau}$ has an important effect on both the stability and the

accuracy of the numerical scheme. Its role has been deeper analyzed for a large number of problems by Cockburn and co-workers, for which see the Ref. [32]. For this work, an appropriate expression for τ has been defined [16], which assumes a diagonal form: $\boldsymbol{\tau} = \tau \boldsymbol{I}$, with $\boldsymbol{I}$ the identity matrix, and depends by the parameters of the simulation (perpendicular and parallel diffusion coefficients, sound speed, size of mesh elements ecc ...).

Eq. C.1 allows to compute the solution $\boldsymbol{U}$ and $\boldsymbol{Q}$ in the entire domain of computation in function of the trace of the unknowns on the element border $\hat{\boldsymbol{U}}$. This variable can be seen as the actual unknown of the problem and it's determined by the setting up of the global problem, which allows to solve for $\hat{\boldsymbol{U}}$ in the whole mesh skeleton. The equation for $\hat{\boldsymbol{U}}$ derives by the imposition of the continuity of the fluxes across the element border. This equation in weak form determines the HDG global problem, and substituting the definition of the fluxes, it is written in this way:

$$\left\langle \hat{\boldsymbol{v}}, \left(\boldsymbol{F} - D_f \boldsymbol{Q} + D_f \boldsymbol{Q}\boldsymbol{b} \otimes \boldsymbol{b} - \boldsymbol{F}_t\right) \boldsymbol{n} + \boldsymbol{\tau}\left(\boldsymbol{U} - \hat{\boldsymbol{U}}\right) \right\rangle_{\partial \mathcal{T}_h \setminus \partial\Omega} + \left\langle \hat{\boldsymbol{v}}, \boldsymbol{B}_{BC} \right\rangle_{\partial\Omega} = 0 \quad \text{(C.2)}$$

where $\boldsymbol{\mathcal{T}}_h$ represents the skeleton of the triangulation, and $\boldsymbol{B}_{BC}$ is a flux vector that defines the boundary condition on $\partial\Omega$, with Ω the computational domain. Here $\hat{\boldsymbol{v}}$ is a vector test function such that $\hat{\boldsymbol{v}} \in \mathcal{P}^p(\partial K)$ with norm $\mathcal{L}^2$, and $\boldsymbol{U}$ and $\boldsymbol{Q}$ are the solutions of the local problem in function of $\hat{\boldsymbol{U}}$. Thus the Eq. C.2 weakly imposes the normal fluxes and it depends only by the unknown $\hat{\boldsymbol{U}}$, reducing the size of the linear system generated by the element discretization.

References

[1] S.H. Kim, J-F. Artaud, V. Basiuk, V. Dokouka, R.R. Khayrutdinov, J.B. Lister, and V.E. Lukash. Plasma current ramp-up phase simulation of iter. *Europhysics Conference Abstracts*, 31(3):2182–2186, 2007.

[2] ITER Physics Expert Group. Plasma operation and control. *Nuclear Fusion*, 39(7):2577–2625, 1999. 12 ITER physics basis.

[3] *ITER Technical Basis*. Number 24 in ITER EDA Documentation Series. INTERNATIONAL ATOMIC ENERGY AGENCY, Vienna, 2002.

[4] Y Gribov, D Humphreys, K Kajiwara, E.A Lazarus, J.B Lister, T Ozeki, A Portone, M Shimada, A.C.C Sips, and J.C Wesley. Chapter 8: Plasma operation and control. *Nuclear Fusion*, 47(6):S385–S403, jun 2007.

[5] J.F. Artaud, V. Basiuk, F. Imbeaux, M. Schneider, J. Garcia, G. Giruzzi, P. Huynh, T. Aniel, F. Albajar, J.M. Ané, A. Bécoulet, C. Bourdelle, A. Casati, L. Colas, J. Decker, R. Dumont, L.G. Eriksson, X. Garbet, R. Guirlet, P. Hertout, G.T. Hoang, W. Houlberg, G. Huysmans, E. Joffrin, S.H. Kim, F. Kchl, J. Lister, X. Litaudon, P. Maget, R. Masset, B. Pégourié, Y. Peysson, P. Thomas, E. Tsitrone,

and F. Turco. The CRONOS suite of codes for integrated tokamak modelling. *Nuclear Fusion*, 50(4):043001, mar 2010.

[6] M. Romanelli, V. Parail, P. da Silva Aresta Belo, G. Corrigan, L. Garzotti, D. Harting, F. Koechl, E. Militello-Asp, R. Ambrosino, M. Cavinato, A. Kukushkin, A. Loarte, M. Mattei, and R. Sartori. Modelling of plasma performance and transient density behaviour in the h-mode access for ITER gas fuelled scenarios. *Nuclear Fusion*, 55(9):093008, aug 2015.

[7] A A Teplukhina, O Sauter, F Felici, A Merle, D Kim, the TCV Team, the ASDEX Upgrade Team, and the EURO fusion MST1 Team. Simulation of profile evolution from ramp-up to ramp-down and optimization of tokamak plasma termination with the RAPTOR code. *Plasma Physics and Controlled Fusion*, 59(12):124004, oct 2017.

[8] V. Lukash, Y. Gribov, A. Kavin, R. Khayrutdinov, and M. Cavinato. Simulations of iter scenarios. *Plasma Devices and Operations*, 13(2):143–156, 2005.

[9] J. Wesson and D.J. Campbell. *Tokamaks*. International Series of Monogr. OUP Oxford, 2011.

[10] R. Simoni, G Corrigan, G Radford, J Spence, and A Taroni. Models and numerics in the multi-fluid 2-d edge plasma code edge2d/u. *Contrib. Plasma Phys.*, 34(2-3):368–373, 1994.

[11] S. Wiesen, D. Reiter, V. Kotov, M. Baelmans, W. Dekeyser, A.S. Kukushkin, S.W. Lisgo, R.A. Pitts, V. Rozhansky, G. Saibene, I. Veselova, and S. Voskoboynikov. The new solps-iter code package. *Journal of Nuclear Materials*, 463:480–484, 2015.

[12] H. Bufferand, G. Ciraolo, Y. Marandet, J. Bucalossi, Ph. Ghendrih, J. Gunn, N. Mellet, P. Tamain, R. Leybros, N. Fedorczak, F. Schwander, and E. Serre. Numerical modelling for divertor design of the WEST device with a focus on plasma–wall interactions. *Nuclear Fusion*, 55(5):053025, apr 2015.

[13] J.A. Soler, F. Schwander, G. Giorgiani, J. Liandrat, P. Tamain, and E. Serre. A new conservative finite-difference scheme for anisotropic elliptic problems in bounded domain. *Journal of Computational Physics*, 405:109093, 2020.

[14] G. Giorgiani, H. Bufferand, G. Ciraolo, P. Ghendrih, F. Schwander, E. Serre, and P. Tamain. A hybrid discontinuous galerkin method for tokamak edge plasma simulations in global realistic geometry. *Journal of Computational Physics*, 374:515–532, 2018.

[15] G. Giorgiani, H. Bufferand, G. Ciraolo, E. Serre, and P. Tamain. A magnetic-field independent approach for strongly anisotropic equations arising plasma-edge transport simulations. *Nuclear Materials and Energy*, 19:340–345, 2019.

[16] G. Giorgiani, H. Bufferand, F. Schwander, E. Serre, and P. Tamain. A high-order non field-aligned approach for the discretization of strongly anisotropic diffusion operators in magnetic fusion. *Computer Physics Communications*, 254:107375, 2020.

[17] A. Gallo, A. Sepetys, Y. Marandet, H. Bufferand, G. Ciraolo, N. Fedorczak, S. Brezinsek, J. Bucalossi, J. Coenen, F. Clairet, Y. Corre, C. Desgranges, P. Devynck, J. Gaspar, R. Guirlet, J. Gunn, C.C. Klepper, J.-Y. Pascal, P. Tamain, E. Tsitrone, E.A. Unterberg, and the WEST team. Interpretative transport modeling of the WEST boundary plasma: main plasma and light impurities. *Nuclear Fusion*, 60(12):126048, nov 2020.

[18] D. Reiter, M. Baelmans, and P. Brner. The eirene and b2-eirene codes. *Fusion Science and Technology*, 47(2):172–186, 2005.

[19] M. Valentinuzzi, Y. Marandet, H. Bufferand, G. Ciraolo, and P. Tamain. Two-phases hybrid model for neutrals. *Nuclear Materials and Energy*, 18:41–45, 2019.

[20] N. Horsten, G. Samaey, and M. Baelmans. Development and assessment of 2d fluid neutral models that include atomic databases and a microscopic reflection model. *Nuclear Fusion*, 57(11):116043, aug 2017.

[21] J. Bucalossi, M. Missirlian, P. Moreau, F. Samaille, E. Tsitrone, D. van Houtte, T. Batal, C. Bourdelle, M. Chantant, Y. Corre, X. Courtois, L. Delpech, L. Doceul, D. Douai, H. Dougnac, F. Fasse, C. Fenzi, F. Ferlay, M. Firdaouss, L. Gargiulo, P. Garin, C. Gil, A. Grosman, D. Guilhem, J. Gunn, C. Hernandez, D. Keller, S. Larroque, F. Leroux, M. Lipa, P. Lotte, A. Martinez, O. Meyer, F. Micolon, P. Mollard, E. Nardon, R. Nouailletas, A. Pilia, M. Richou, S. Salasca, and J.-M. Travre. The west project: Testing iter divertor high heat flux component technology in a steady state tokamak environment. *Fusion Engineering and Design*, 89(7):907–912, 2014. Proceedings of the 11th International Symposium on Fusion Nuclear Technology-11 (ISFNT-11) Barcelona, Spain, 15-20 September, 2013.

[22] H. Bufferand, P. Tamain, S. Baschetti, J. Bucalossi, G. Ciraolo, N. Fedorczak, Ph. Ghendrih, F. Nespoli, F. Schwander, E. Serre, and Y. Marandet. Three-dimensional modelling of edge multi-component plasma taking into account realistic wall geometry. *Nuclear Materials and Energy*, 18:82–86, 2019.

[23] P. C. Stangeby. *The Plasma Boundary of Magnetic Fusion Devices (1st ed.)*. CRC Press, Boca Raton, 2000.

[24] M. Valentinuzzi, G. Giorgiani, Y. Marandet, H. Bufferand, G. Ciraolo, P. Tamain, E. Serre, and Ph. Ghendrih. Fluid description of neutral particles in divertor regimes in west. *Contributions to Plasma Physics*, 58(6-8):710–717, 2018.

[25] Shinji Nakazawa, Noriyoshi Nakajima, Masao Okamoto, and Nobuyoshi Ohyabu. One-dimensional simulation on stability of detached plasma in a tokamak divertor. *Plasma Physics and Controlled Fusion*, 42(4):401–413, mar 2000.

[26] J.D. Huba, D.L. Book, and Naval Research Laboratory (U.S.). *NRL Plasma Formulary*. NRL publication. Naval Research Laboratory, 1998.

[27] G. Giorgiani, T. Camminady, H. Bufferand, G. Ciraolo, P. Ghendrih, H. Guillard, H. Heumann, B. Nkonga, F. Schwander, E. Serre, and P. Tamain. A new high-order fluid solver for tokamak edge plasma transport simulations based on a magnetic-

field independent discretization. *Contributions to Plasma Physics*, 58(6-8):688–695, 2018.

[28] A. Paredes, H. Bufferand, G. Ciraolo, F. Schwander, E. Serre, P. Ghendrih, and P. Tamain. A penalization technique to model plasma facing components in a tokamak with temperature variations. *Journal of Computational Physics*, 274:283–298, 2014.

[29] Ph Ghendrih, K Bodi, H Bufferand, G Chiavassa, G Ciraolo, N Fedorczak, L Isoardi, A Paredes, Y Sarazin, E Serre, F Schwander, and P Tamain. Transition to supersonic flows in the edge plasma. *Plasma Physics and Controlled Fusion*, 53(5):054019, apr 2011.

[30] A Gallo, A Sepetys, J Romazanov, Y Marandet, S Brezinsek, H Bufferand, G Ciraolo, Y Corre, S Ertmer, N Fedorczak, J Gunn, A Kirschner, C Martin, O Meyer, G J van Rooij, P Roubin, E Tsitrone, the EUROfusion PFC team, and the WEST team. First efforts in numerical modeling of tungsten migration in WEST with SolEdge2d-EIRENE and ERO2.0. *Physica Scripta*, T171:014013, jan 2020.

[31] Y. Marandet, H. Bufferand, J. Bucalossi, G. Ciraolo, S.W. Lisgo, and E. Tsitrone. Assessment of tungsten sources in the edge plasma of west. *Journal of Nuclear Materials*, 463:629–633, 2015.

[32] N.C. Nguyen, J. Peraire, and B. Cockburn. An implicit high-order hybridizable discontinuous galerkin method for nonlinear convectiondiffusion equations. *Journal of Computational Physics*, 228(23):8841–8855, 2009.